UNIVERSITÀ DEGLI STUDI DI PADOVA
Dipartimento di Fisica e Astronomia "Galileo Galilei"

Master Degree in Astrophysics and Cosmology

Final Dissertation

Interferometric measurements and data analysis for the study of thermal noise in solids

Thesis supervisor
Prof. Giacomo Ciani
Thesis co-supervisors
Dr. Livia Conti
Dr. Luis Diego Bonavena

Candidate
Giulia Saoncella

Academic Year 2022/2023

Contents

Introduction

Thermal noise constitutes a fundamental limitation to sensitivity in high precision experiments. While well understood at thermodynamic equilibrium, where it is modeled by means of the fluctuation-dissipation and equipartition theorem, it has not been properly modeled in non-equilibrium conditions yet. An example of the importance of the study of thermal noise out of equilibrium is provided by gravitational waves detectors: for the purpose of estimating the impact of thermal noise on their performance, these experiments are usually modeled as equilibrium systems from a thermodynamic point of view; however, the validity of this assumption is questionable for a variety of reasons. Temperature gradients are often present in these systems, as for example in mirror coatings and mirror suspensions, which exhibit non-uniform temperatures due to heat fluxes generated by the absorbed laser power, by thermal compensation techniques and, especially in future detectors, by the need to operate the mirrors at cryogenic temperatures.

The Non-Equilibrium Thermal Noise (NETN) experiment aims to experimentally investigate thermal noise in and out of thermodynamic equilibrium, by studying its effects on a macroscopic aluminum oscillator, consisting of a rod with a cubic mass at the end, placed in a vacuum environment and isolated from external noise sources by a system of mechanical filters. The thermal noise-induced vibrations are measured on the oscillator through a quadrature phase differential interferometer. The final goal is to provide a phenomenological relation between the thermal noise level and the parameters that characterize the non-equilibrium condition.

As a preliminary step, this work focuses on acquiring and analyzing the interferometric output in thermodynamic equilibrium, in order to measure thermal noise in accordance with the fluctuation-dissipation theorem, with the future goal of studying its behavior outside thermodynamic equilibrium.

Chapter 1 introduces the topic of gravitational waves and their detection. The main noise sources limiting the sensitivity of gravitational waves interferometers are illustrated. Particular attention is given to the critical topic of thermal noise, both in and out of thermodynamic equilibrium. Chapter 2 illustrates the components of the NETN experimental apparatus. Chapter 3 describes the interferometric readout and the spectral analysis carried out on it to obtain thermal noise measuremements. Chapter 4 finally presents the experimental results of this work, focused on the measure of thermal noise in thermodynamic equilibrium.

Chapter 1

Gravitational Waves Detectors and Thermal Noise

This first chapter introduces the context of gravitational waves (section 1.1) and the apparatus designed for their detection (section 1.2). This section assumes a basic understanding of gravitational waves physics. While a concise overview is provided, a complete discussion about the topics here covered can be found in the book *Gravitational Waves - Volume 1 - Theory and Experiments* of Michele Maggiore [11]. Section 1.3 illustrate the different noise sources that affect the GW interferometers sensitivity. Special emphasis is placed on the critical consideration of thermal noise originated in the mirror coatings and in the mirror suspensions of GW detectors, in which the present work aims to find an application. Section 1.4 addresses the problem of thermal noise outside thermidynamic equilibrium, as in the case of GW detectors, and presents previous studies on this topic.

1.1 Gravitational Waves

Gravitational waves (GW) are disturbances in the curvature of space-time that propagate as waves at the speed of light, generated by the acceleration of asymmetric mass distributions in a strong gravitational field. GW signals are expected in a wide range of frequencies: from the order of $\sim 10^{-17}$ Hz of the ripples in the cosmological background, to the formation of neutron stars in supernovae explosions, with a frequency of the order of $\sim 10^3$ Hz. The principal issue of their detection lies in the amplitude of these signals: the predicted magnitude of a strain caused by a GW, as measured on Earth, is of the order of 10^{-21} or lower [9].

Gravitational waves were predicted by Albert Einstein's general theory of relativity in 1915. The formalism for the generation of gravitational waves in general relativity was published by Einstein in (1916) [1]. In this work, Einstein linearized his field equations to describe weak gravitational fields and derived the quadrupole formula, which predicts the emission of gravitational waves by systems with changing quadrupole moments:

$$h_{ij} = \frac{2G}{c^4}\frac{d^2 I_{ij}}{dt^2} \tag{1.1}$$

where h_{ij} represents the amplitude of the metric perturbation caused by the gravitational wave, G is the gravitational constant, c is the speed of light and I_{ij} is the trace-free quadrupole moment tensor which describes the distribution of mass within a system. It is useful for the comprehension of the topics covered in the following paragraphs to express the amplitude h_{ij} in the transverse-traceless gauge, for a gravitational wave propagating in the z direction:

$$h_{ij}(t,x,y,z) = \begin{pmatrix} 0 & 0 & 0 & 0 \\ 0 & h_+ & h_\times & 0 \\ 0 & h_\times & -h_+ & 0 \\ 0 & 0 & 0 & 0 \end{pmatrix} \tag{1.2}$$

where h_+ is the plus-polarization gravitational wave strain and $h_\times$ is the cross-polarization strain. In this gauge choice the trace of the matrix in equation 1.2 is zero, and the space-time strain is only in the x and y directions, transverse to the z direction of propagation. The space-time distortion caused on a set of masses placed in circle by a plus-polarized GW and a cross-polarized GW can be seen in figure 1.1.

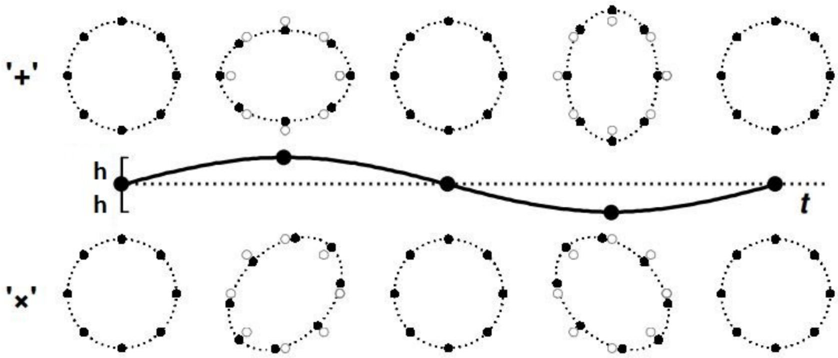

Figure 1.1: Illustration of the space-time distortion caused on a set of masses placed in circle by a plus-polarized GW (up) and a cross-polarized GW (down) impinging perpendicularly to the plane of the circle. The stretching and squeezing encountered across the GW path takes place in the perpendicular plane to the GW direction. The distortion caused on the free mass is dependent not only on the GW polarization but also its amplitude (strain) and frequency. Picture from [26].

The quadrupole formula (1.1) shows how a changing mass distribution, characterized by a non-zero second time derivative of the quadrupole moment, leads to the emission of gravitational waves. This formula is particularly relevant for systems like binary stars, where the masses are in motion, causing a dynamic change in the system quadrupole moment. As the masses accelerate, gravitational waves are generated and propagate through spacetime, carrying away energy and causing the orbits of the masses to decay. As the binary system approaches closer distances, the orbital period decreases, and the rate of energy loss through GW emission intensifies. The system enters a critical phase known as the final plunge, where the GW become more frequent and powerful. During this phase, the masses experience an accelerated inspiral, culminating in the coalescence of the binary system.

1.2 Gravitational Waves Detectors

Despite Einstein's theoretical prediction, the physical reality of gravitational waves was initially met with skepticism. Einstein himself initially had doubts about the physical reality of gravitational waves. Moreover, the weak coupling of gravitational waves with matter posed a considerable experimental challenge, leading some scientists to question the feasibility of detection. It wasn't until the 1960s that physicists like Joseph Weber began experimental efforts to directly detect these waves using resonant bar detectors [2].

The indirect evidence for the existence of gravitational waves came from observations of binary pulsars. In 1974, Russell Hulse and Joseph Taylor discovered a binary pulsar system, PSR

B1913+16, which exhibited a gradual orbital decay [3]. The observed decay matched the predictions of general relativity for the energy loss due to gravitational wave emission, providing strong indirect evidence for the existence of these waves.

The first direct detection of gravitational waves, as predicted by Einstein, was finally achieved in 2015 by the Laser Interferometer Gravitational wave Observatory (LIGO) with the observation of a binary black hole merger [4].

1.2.1 Resonant Bar Detectors

The first experiments in the field of GW detection were the ground based resonant bar detectors, developed by physicist Joseph Weber of the University of Maryland in the 1960s. They represent an early approach in the attempt to directly detect gravitational waves.

The principal idea behind the detector is to observe the resonant bar modes being excited by the transiting GW. Each mode can be studied independently, but the most relevant one is the lowest longitudinal mode, since it is characterized by the higher quadrupole moment and thus it is the most affected by GW energy transfer. It represents the frequency the bar is most sensible to. The size and composition of the bar are crucial factors, as they determine the natural frequencies at which the bar can resonate.

The main limit to sensitivity in this type of detector was thermal noise. In fact the average amplitude of the resonant bar oscillation due to thermal fluctuations was many orders of magnitude larger than the expected oscillation amplitudes induced by a transiting GW. The solution Weber adopted to overcome the problem was to use materials with a high mechanical quality factor $Q = \omega\tau_E$, where τ_E is the energy relaxation time (maximum stored energy over the dissipated power) and ω is the angular frequency at which the stored energy and power loss are measured. High-Q materials enable the resonant bar to "ring" at its natural frequency for an extended period, even in the presence of thermal noise. This extended resonance time provides a more significant window for detecting the subtle changes induced by passing GW. As a result, the use of high-Q materials enhances the detector's sensitivity, allowing it to pick up weak GW signals that might otherwise be masked by thermal noise.

Weber's first large suspended bar antenna was built out of aluminum, since it constitutes a high quality factor oscillator. It was a 1.2 ton aluminum cylinder of length ~1.5 m and diameter ~61 cm, suspended in a vacuum chamber on acoustic filters, with the first longitudinal mode resonating at 1657 Hz (at room temperature) [2]. In 1969 Weber announced the detection of a GW signal, but in the following years more sensitive resonant bar experiments, including low-temperature bars, were never able to replicate his results and to confirm the presence of GW of the amplitude implied by Weber's data.

Over the year many other resonant bar detectors have been built, with a significant emphasis on cooling to reduce thermal noise levels, reaching sensitivities four order of magnitude higher in energy. NAUTILUS, EXPLORER and AURIGA were among those that achieved the best performance in terms of sensitivity. NAUTILUS (figure 1.2 (a)) and AURIGA (figure 1.2 (b)), built in Italy (respectively in Frascati, Rome and Legnaro, Padua, where also the NETN experiment (2) is located), were the only two ultracryogenic bar antennae that ever went into operation (cooled at 130 and 200 mK respectively), while EXPLORER was a low-temperature bar (2.6 K) located at CERN (Geneva). AURIGA, EXPLORER and NAUTILUS had a triple overlapping operation in 2005 with about 72% of duty cycle.

Figures 1.3, and 1.4 from [2] shows the sensitivity curves of the three bar detectors. These curves result from the sum of thermal noise (magenta and sky blue curves), amplifier noise (green) and quantum back action noise (yellow). The cooling of the antenna therefore did not necessarily improved the sensitivity curve if thermal noise were not dominant in the considered bandwidth.

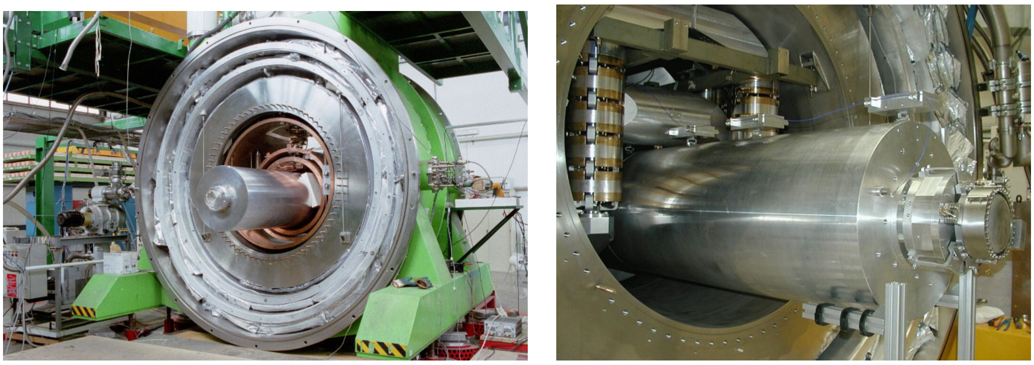

(a) *NAUTILUS resonant bar detector* (b) *AURIGA resonant bar detector*

Figure 1.2: (a) NAUTILUS gravitational wave detector, consisting of a 2.3 ton resonant bar at a temperature of 0.13 K, located at the Frascati Laboratories (Rome). (b) AURIGA gravitational wave detector, consisting of a 3-meter aluminum cylinder, cooled at 0.2 K, located at the Laboratori Nazionali di Legnaro (Padua).

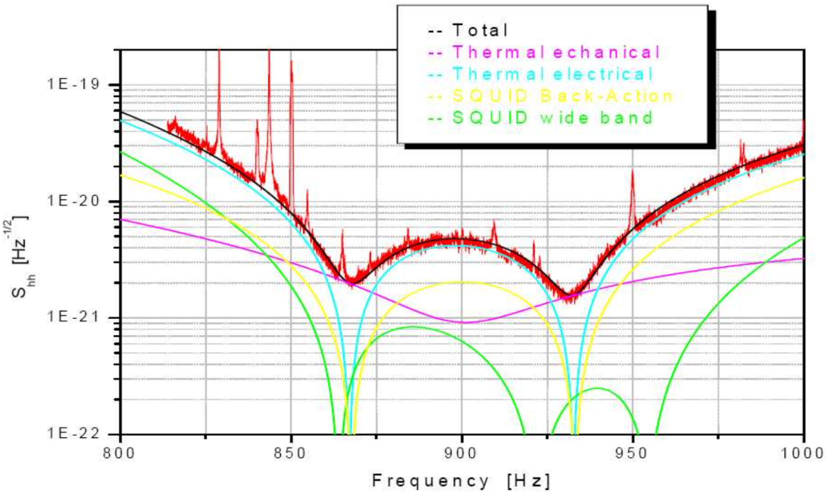

Figure 1.3: Power spectral density of the AURIGA detector operating a 4.5 K, using a two stage low noise dc-SQUID amplifier. The black curve represents the predicted value while the red curve represents the experimental one. The dominating noise source is the electrical resonator thermal noise (sky blue curve) except at the resonances, where the antenna thermal noise dominates. Picture from [2].

Cryogenic resonant bars made no confirmed detections, and around 2003 the sensitivity of km-scale GW interferometers began to surpass their peak sensitivity. Moreover, interferometric detectors demonstrated to be sensible to a much broader range of frequencies with respect to the resonant bars, which were limited to the narrow band around their resonant frequencies.

1.2.2 Gravitational Waves Interferometers

Gravitational waves interferometers are based on the Michelson interferometer concept. A simple scheme of a Michelson interferometer is shown in figure 1.5. In its simplest configuration, a laser beam is split by a beam splitter and sent along the two perpendicular arms of the interferometer of length L. Higly reflective mirrors, also called test masses, are placed at the end of the interferometer

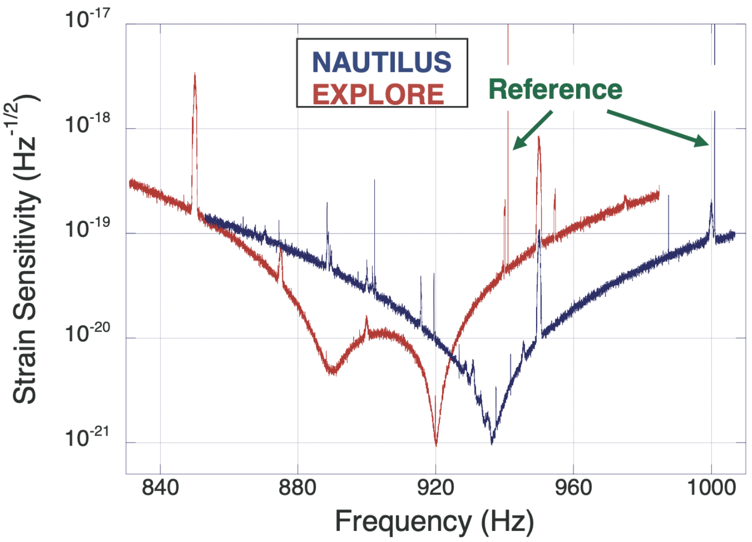

Figure 1.4: Power spectral density of NAUTILUS and EXPLORER detectors. Picture from [2].

arms and suspended from pendulums. Laser interferometry is used to keep track of the test mass motion, possibly caused by a transiting GW. For example, a GW wave propagating perpendicular to the plane of the interferometer, and with a polarization whose axis correspond to those of the interferometer's arms, will cause a space-time distortion resulting in one arms of the interferometer being increased in length and the other decreased, as schematically described in figure 1.1 (equivalently, this can be seen as a change in the proper travel time of photons). The GW effect can be identified thus with a strain $h = \Delta L/L$, where ΔL is the path length difference between the two arms of the interferometer. This path length difference translates in a small change of the light intensity observed at the interferferometer output, read by a photodetector, which indicates the transit of a GW.

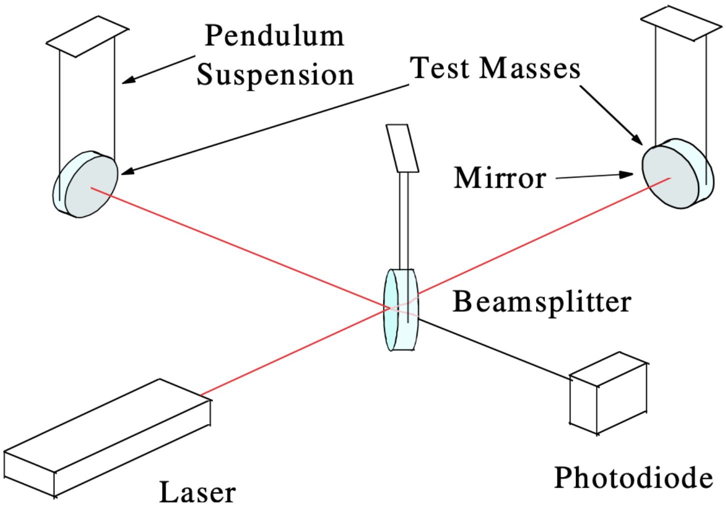

Figure 1.5: Simplified scheme of a gravitational wave interferometer. Picture from [9].

The functioning of a GW interferometer can be explained in a simple way as follow. By considering the electro-magnetic field of the laser to be propagating along the z-axis, the input laser light can be described in complex notation (where vector quantities are indicated in bold) as:

$$\boldsymbol{E(z)} = E_0 e^{i(kz-\omega_L t)} \tag{1.3}$$

where E_0 is the amplitude of the laser beam entering the interferometer, ω_L is the laser frequency, $k = \frac{2\pi}{\lambda}$ is the wave vector and λ the laser wavelength. Before entering the interferometer, the laser intensity is equal to $I_{in} \propto EE^* = |E|^2$. When the laser encounter the 50:50 beam splitter, it is divided in two different beams, $\boldsymbol{E_1}$ and $\boldsymbol{E_2}$. These fields propagate along the two perpendicular arms of the interferometer, of length L_1 and L_2 respectively. The two beams reach the end mirrors (M_1 and M_2) and are reflected back towards the beam splitter, where they recombine. The two beams, just before the recombination into the beam splitter, can be described as:

$$\boldsymbol{E_1(z)} = \frac{1}{2} E_0 e^{i(kz-\omega_L t)} e^{(i2kL_1)} \tag{1.4}$$

$$\boldsymbol{E_2(z)} = \frac{1}{2} E_0 e^{i(kz-\omega_L t)} e^{(i2kL_2)} \tag{1.5}$$

where the terms $e^{(i2kL_1)}$ and $e^{(i2kL_2)}$ indicate the phase accumulated by the two beams while propagating along the two perpendicular arms. Once $\boldsymbol{E_1}$ and $\boldsymbol{E_2}$ recombine at the beam splitter, the resulting beam is directed towards the photodetector, which reads its intensity I_{out}, resulting from the interference of the two beams. The intensity of the outgoing beam, read by the photodetector, is:

$$I_{out} \propto |E_{out}|^2 = |E_1 + E_2|^2 = \frac{1}{2} E_0^2 - \frac{1}{2} E_0^2 cos[2k(L_2 - L_1)] = \frac{1}{2} I_{in} [1 - cos(2k\Delta L)] \tag{1.6}$$

where $2k\Delta L = \Delta\phi$. Therefore any variation of the length of a arm, such the one caused by the transit of a GW, results in a corresponding variation of the power read by the photodetector.

When this is applied to the detection of GW of course the functioning is not that simple: a general relativistic computation from [11] demonstrates that the phase difference induced by a $+$ polarized GW of amplitude h_0, propagating along z, to the laser beam traveling along the two perpendicular arms of an interferometer, if these lies on the x and y-axis, is:

$$\Delta\phi_{gw} = \omega_L \frac{2L}{c} h_0 cos\left(\omega_{gw} t + \frac{L}{c}\right) sinc\left(\frac{\omega_{gw} L}{c}\right) \tag{1.7}$$

where L of the interferometer arms and ω_{gw} is the grabitational wave frequency. This derivation applies to a GW propagating along z and plus-polarized. In this case the other $\times$ polarization is completely invisible to the detector, since it would cause a simultaneous and equal change on the two arms.

In a more generic way, the strain caused on the detector by a gravitational wave emitted by a source at spherical coordinates (θ, ϕ) can be derived applying two rotational matrices to the $+$ and $\times$ polarization components of the GW, thus calculating the so called antenna pattern:

$$h(t) = \frac{1}{2}(1 + cos^2(\theta)) cos(2\phi) h_+(t) + cos(\theta) sin(2\theta) h_\times(t) \tag{1.8}$$

where θ is the polar angle and ϕ the azimuthal angle. The polarization angle ψ, which indicate the rotation of the GW coordinate system relative to the interferometer reference frame (see figure 1.6 for a reference), is considered here equal to 0. The antenna pattern response functions for the h_+ and $h_\times$ GW polarizations (see figure 1.1) are shown in figure 1.7.

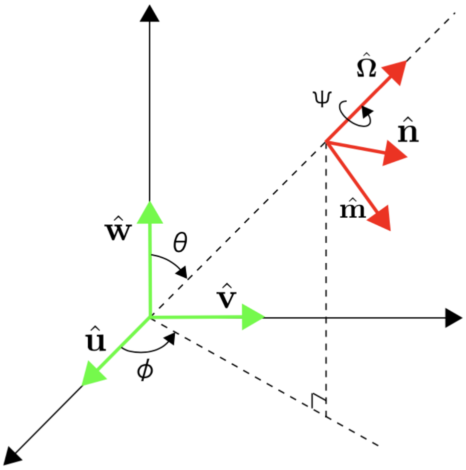

Figure 1.6: Detector coordinate system ($\hat{u}$, $\hat{v}$, $\hat{w}$) in green and gravitational-wave coordinate system ($\hat{m}$, $\hat{n}$, $\hat{\Omega}$). Picture from [12].

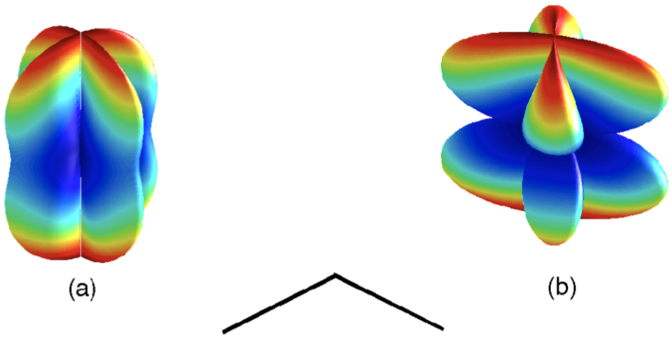

Figure 1.7: Antenna pattern response functions of an interferometer. Images (a) and (b) show the + and × antenna pattern function. Color indicates the strength of the response, with red being the strongest and blue being the weakest. The black lines between the two pictures give the orientation of the interferometer arms. Picture from [12].

From equation 1.7 it can be seen that for a GW of a given frequency ω_{gw}, the dependence on L is given by a factor $(\omega_L L/c) sinc(\omega_{gw} L/c) = (\omega_L/\omega_{gw}) sin(\omega_{gw} L/c)$. Therefore, the optimal arm length to maximize the interferometer response to the GW is given by $\omega_{gw} L/c = \pi/2$, i.e. $L = \lambda_{gw}/4$. In therms of $f_{gw} = \omega_{gw}/(2\pi)$, this gives:

$$L \simeq 750\, km \left(\frac{100\, Hz}{f_{gw}}\right) \tag{1.9}$$

Obviously arms of hundreds of kms are not feasible to build in a ground-based interferometer, both for practical and financial reasons (considering also that, among other things, the interferometer arms should be enclosed in a high vacuum system).

Modern GW interferometers like two LIGO ones (Hanford and Livingston, USA) and VIRGO (Pisa, Italy) have arms respectively 4 and 3 km long. A picture of these three interferometers is shown in 1.8.

(a) *LIGO interferometer in Hanford (Washingtone, USA)*

(b) *LIGO interferometer in Livingston (Louisiana, USA)*

(c) *VIRGO interferometer in Cascina (Pisa, Italy)*

Figure 1.8: Pictures of the three currently active ground-based interferometers.

The idea is to not increase the physical arm length but their effective length by "folding" the optical path of the laser, making it bounce back and forth many times in each arm before recombining the two beams. Two different design were considered for this purpose: to build the so called "delay lines", or to use optical cavities.

In the first one, the laser light goes back and forth along trajectories that do not superimpose, and which hit different point on the mirrors. The problem with this scheme was the need of unpractical large mirrors, since to reach the necessary path length of ~750 km the number of bounces needed is of the order of $O(100)$.

In the second design, which is the one adopted in the modern GW interferometers such LIGO and VIRGO, each arm is transformed into a Fabry-Pérot cavity, where each photon still bounces back and forth between the two cavity mirrors, but it is bounced back on its own path. In this way the photons effectively travel a much longer distance before going back to the beam splitter. The high power build-up inside the cavities is also necessary to overcome limitations to the detector sensitivity due to photon shot noise (mentioned in more detail in section 1.3).

An example of delay lines and Fabry-Pérot cavities implementation on a GW interferometer is schematically shown in figure 1.9.

Many other improvements to the simple Michelson interferometer design are applied in modern

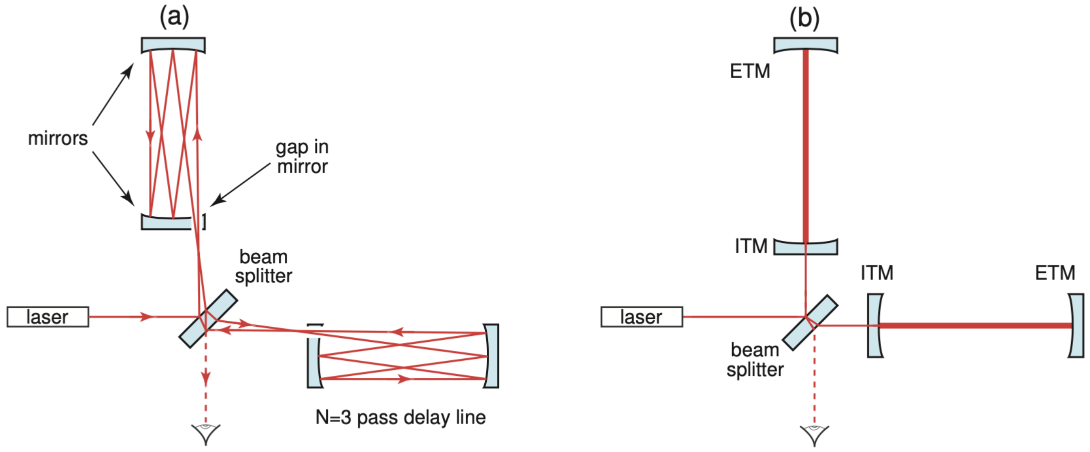

Figure 1.9: Example of Michelson interferometers with (a) delay lines and (b) Fabry–Pérot cavities as the arms of the interferometer. Picture from [9].

interferomeners, such as a power recycling cavity, used to increase even more the effective power in the interferometer arms, or input and output mode cleaners, used to reject higher order modes and to stabilize the laser frequency. A more detailed description of these techniques can be found in [10].

1.3 Noise Sources in Gravitational Waves Interferometers

Gravitational wave interferometers are highly sensitive instruments designed to detect the faintest perturbations. However, their sensitivity makes them susceptible to various noise sources that compromise their performance. Understanding and mitigating these noise sources is essential for optimizing signal detection. As an example, the sensitivity curve of the VIRGO interferometer is show in figure 1.10, built considering the limitations imposed by the various noise sources. The types of noise that most affect GW detectors are briefly described below, paying particular attention to thermal noise, on which the present work is focused.

1.3.1 Seismic Noise

Seismic noise refers to the vibrations and movements of the Earth crust caused by various natural and human sources and can impact GW interferometers by displacing the mirrors and misaligning the optical components, inducing vibrations of the order of $O(10^{-6}m)$ on the detector components.

Seismic noise can be managed in a passive or active way: the first consist in choosing geologically stable locations to minimize ground motion and utilize suspension systems and isolation platforms that isolate sensitive optical components from ground vibrations. An active way to deal with seismic noise is to employ seismic isolation systems that actively counteract ground motion, reducing its transmission to the interferometer sensitive elements. Signal processing techniques are also applied to the data to identify and filter out noise from seismic sources.

1.3.2 Newtonian Noise

Newtonian noise consists in gravity gradients (stochastic fluctuations of the local gravitational field) that are generated by seismic vibrations or variations in the atmospheric pressure.

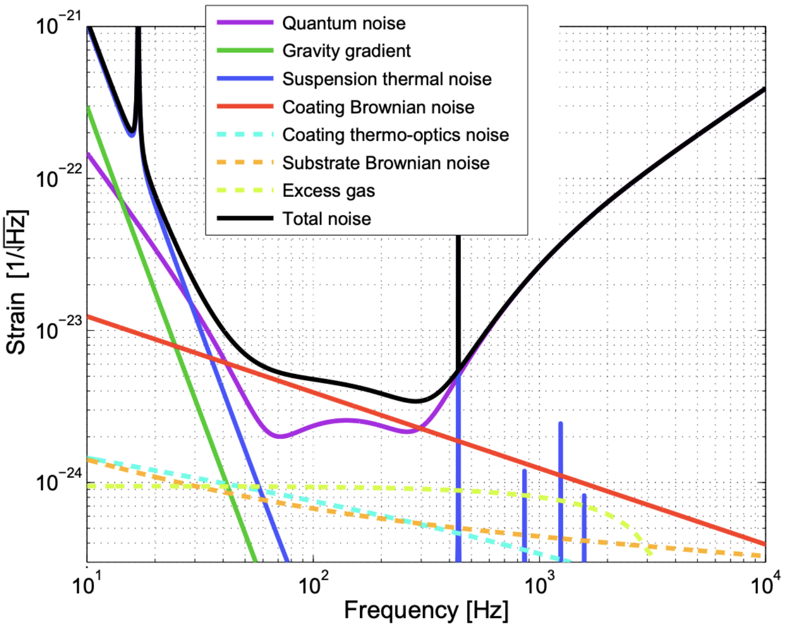

Figure 1.10: Advanced Virgo sensitivity curve. The noise level on the y-axis is given in equivalent GW amplitude that has the same physical nature of strain. Picture from [13].

Since newtonian noise consists in gravitational field variations, it mimics gravitational waves, and can not therefore be shielded without shielding GW as well. An active strategy to deal with newtonian noise is to deploy a network of sensor measuring ground displacement and atmospheric variations, in order to model its effect on the mirrors and subtract it from the GW signal. A passive strategy consists in choosing a very quiet location, as in the case of seismic noise, and to go underground. Since the dominant source of gravity-gradient noise are surface waves, the observed noise decreases with depth into the Earth.

1.3.3 Quantum Noise

Quantum noise can be divided into two contributions: shot-noise and radiation pressure noise.

Shot noise arises due to the discrete nature of light, which is composed of individual photons. The arrival of each photon at the photodetector is a stochastic event, leading to statistical fluctuations in the observed signal known as shot noise. The number of photons arriving on the photodetector in a time τ obeys Poisson statistics and it can be shown that the detectable strain sensitivity depends on the laser power P as $S_{h,shot}^{1/2} \sim \frac{1}{\sqrt{P}}$ [9], thus increasing the power P of the laser can help mitigate shot noise.

On the other hand, photons impinging on the test mass and exchanging momentum with it are associated with a stochastic force called quantum radiation pressure noise. As the effective laser power in the arms is increased, the magnitude of the force, and of its fluctuations, is also increased; thus the detectable strain sensitivity limited by radiation pressure noise is $S_{h,rp}^{1/2} \sim \sqrt{P}$ [9].

Radiation pressure may be a significant sensitivity limitation at low frequency. Its effects could be reduced by increasing the mass of the mirrors or decreasing the laser power, but at the expenses of the shot noise at higher frequencies. For a given frequency, it can be identified an optimum laser power which minimizes the effect of these two sources of quantum noise. Given that shot noise and radiation pressure noise have opposite proportionality to the laser power, for a given frequency f a fundamental limit exists to the displacement sensitivity, known as the Standard Quantum Limit (SQL):

$$S^{1/2}_{h,SQL}(f) = \frac{1}{2\pi f L}\sqrt{\frac{8\hbar}{M}} \tag{1.10}$$

where L is the arm length and M the mirrors mass.

1.3.4 Thermal Noise

Thermal noise is one of the most significant noise source affecting GW interferometers at the low-mid frequency band, as can be seen in figure 1.10. It is originated in the mirror coatings (thin layers of materials applied to the surface of a mirror to modify its reflective properties) and in the mirror suspensions, in general contributed by any source of dissipation, internal or external.

Thermal noise is fundamentally due to the thermal kinetic energy of the atoms that compose the mirror coating and mirror suspensions. Weber realized that, in a mechanical oscillator with high Q-factor, the minimum GW energy that could be detected was much smaller, since it persisted in the oscillator much longer. Therefore by averaging over a long time, the GW energy could be distinguishable from the thermal one. To demonstrate this physical intuition it is useful to study the evolution of the resonant bar fundamental mode ξ_0 in the presence of thermal noise. The evolution of ξ_0 is studied by [11] using the equation for a damped oscillator:

$$\ddot{\xi_0} + \omega_0^2 \xi_0 = -\gamma \dot{\xi_0} \tag{1.11}$$

where ω_0 is the resonance frequency of the fundamental mode and γ the dissipation coefficient. If this was the complete description of the bar dynamics, so without the presence of thermal noise, the time evolution of $\xi_0(t)$ could be described in a fully deterministic way.

This is not the case: thermal noise acts as a stochastic force, which can be described only in a statistical way. It is responsible both for the dissipation term $-\gamma\dot{\xi_0}$ and for the fluctuations around it. Considering also these fluctuations, 1.11 can be rewritten as:

$$m(\ddot{\xi_0} + \omega_0^2 \xi_0) = F_{th} \tag{1.12}$$

with m the oscillator mass and F_{th} is the stochastic force describing the thermal fluctuations around the equilibrium, called Nyquist Force. These fluctuations, as said before, are described as a stochastic Gaussian process, so that by definition $\langle F_{th}(t)\rangle = 0$, where the angular brackets denote a time average, since they are the sum of many independent contributions. On a macroscopic time-scale this force at a time t is completely uncorrelated with itself at a different time t'.

The relation between the single-sided spectral density $S_{F_{th}}(\omega)$ of the force $F_{th}(t)$, representing the stochastic fluctuations due to thermal noise, and the dissipation (γ) is derived by [11] to be:

$$S_{F_{th}}(\omega) = 4k_B T\gamma \tag{1.13}$$

where k_B is the Boltzmann constant and T the equilibrium temperature. This obtained relation represents a particular case of the Fluctuation-Dissipation Theorem (FTD). The FTD can be formulated considering $x(t)$ to be the variable describing a linear system, subject to an external force F(t), and $v(t) = \dot{x}(t)$ the velocity. In Fourier space, the equation of motion can always be expressed in the general form:

$$\tilde{F}(\omega) = Z(\omega)\tilde{v}(\omega) \tag{1.14}$$

where $Z(w)$ is the impedance of the system. The FDT states that the single-sided power spectrum of the force causing the thermal fluctuations, denoted $S_F(\omega)$, can be defined in function of the real part of the system impedance Z:

$$S_F(\omega) = 4kTRe[Z(\omega)] \tag{1.15}$$

It is useful for the comprehension of the present work to study the motion of a particle, subject to velocity damping (VD), to a Hooke restoring force and to thermal noise [15]:

$$m\ddot{x}(t) + \gamma\dot{x}(t) + kx(t) = F_{th}(t) \tag{1.16}$$

where m is the mass of the particle, γ the velocity damping coefficient and k the spring constant of the restoring force F_s. The thermal noise spectrum in case of velocity damping can be computed using 1.15 after calculating the impedance $R(\omega)$ as follows:

$$R(\omega)_{th,VD} = Re\left[\frac{F}{\dot{x}}\right] = Re\left[\frac{\ddot{x} + \gamma\dot{x} + kx}{\dot{x}}\right] = Re\left[i\omega m + \gamma + \frac{k}{i\omega}\right] = \gamma \tag{1.17}$$

The spectrum of the thermal force is then equal to $S_{F_{th,VD}}(\omega) = 4k_BT\gamma$, as found in 1.13, thus thermal noise results to be a white noise in the case of a particle velocity damping, not depending on frequency.

The power spectral density (PD) of the particle motion $S_x(\omega)$ induced by thermal noise can be computed by first writing equation 1.16 in the frequency domain:

$$x(\omega) = \frac{1}{-m\omega^2 + i\omega\gamma + k}F_{th,VD}(\omega) = H(\omega)F_{th(\omega)} \tag{1.18}$$

where $H(\omega)$ is the thermal noise transfer function. The PSD of the oscillating mass position is then:

$$S_{x,VD}(\omega) = |H(\omega)|^2 S_{F_{th,VD}}(\omega) = \frac{4k_BT\gamma}{(k - m\omega^2)^2 + (\omega\gamma)^2} = \frac{4k_BT}{mQ\omega_0}\frac{1}{\left(1 - \frac{\omega^2}{\omega_0^2}\right)^2 + \left(\frac{\omega}{Q}\right)^2} \tag{1.19}$$

where $S_{F_{th}}$ is the power spectral density of the thermal driving force and in the third equality the definitions $\gamma = m\omega_0/Q$ and $k = m\omega_0^2$ have been used.

When this description is applied to a solid, as in the present work, the damping is modeled as internal (ID), which can be expressed by writing the restoring force in function of a complex spring constant [15]:

$$F_s = -k(1 + i\phi(\omega))x. \tag{1.20}$$

The imaginary component of the spring constant causes a time lag between the applied thermal force and the response of the spring. A fraction $2\pi\phi(\omega)$ of the energy stored in the oscillatory motion is dissipated at each cycle [15]. The PSD of the thermal driving force in the case of internal damping is equal to:

$$S_{F_{th},ID}(\omega) = 4k_BTk\phi(\omega)\omega^{-1} \tag{1.21}$$

which is not anymore white, as in the case of velocity damping. Therefore the PSD of the position of a solid subject to internal damping can be calculated as:

$$S_{x,ID}(\omega) = |H(\omega)|^2 S_{F_{th,ID}}(\omega) = \frac{4k_BTk\phi(\omega)}{\omega[(k-m\omega^2)^2 + (k\phi(\omega))^2]} = \frac{4k_BT}{\omega\omega_0^2 mQ}\frac{1}{\left(1-\frac{\omega^2}{\omega_0^2}\right)^2 + \left(\frac{1}{Q}\right)^2} \tag{1.22}$$

where in the last equality the definition of internal damping quality factor $Q = 1/\phi(\omega_0)$ is been used [15]. The sharpness of the resonance in the PSD of the position is determined by the quality factor Q, defined as $Q = \omega_0/\Delta\omega$, where ω_0 is the resonance frequency and $\Delta\omega$ is the full width at half maximum (FWHM). For low-loss systems or materials (high-Q) the PSD of the position has a sharp peak around ω_0.

It is useful for the topics covered in the next sections to report the estimation, from the integral of the spectra 1.19 and 1.22, of the mean square displacement of the mass $\langle x_{th}^2\rangle$ caused by thermal noise. At thermodynamic equilibrium and in absence of external noises, the law of equipartition states that:

$$\langle x_{th}^2\rangle = \frac{k_BT}{m\omega_0^2} \tag{1.23}$$

1.4 Thermal Noise Out of Thermodynamic Equilibrium

Currently thermal noise affecting GW interferometers is modeled by means of the FDT, assuming the systems to be at thermodynamic equilibrium. Thermal noise prediction that uses the FDT are well verified in high-precision experiments characterized by a thermodynamic equilibrium situation, but for many reasons GW interferometers can not be considered equilibrium devices. There are in fact many process and components that drive the detector out of the equilibrium state [20], such as the light power dissipated into the mirror substrates and coatings, the external additional thermal load used to deform the mirrors in order to create the desired radius of curvature and many others.

If non-equilibrium states processes are proven to be significant in a GW interferometer, they need to be considered in the modeling of the noise statistics, since the latter could be intrinsically different from the equilibrium Gaussian statistics.

However, up until now, there is no complete theory in statistical mechanics describing thermal noise in solids out of thermodynamic equilibrium. Given that GW detectors are constantly developing improvements to increase sensitivity to GW signals, many of which concerns higher circulating powers or the use of cryogenic temperatures, it is of fundamental importance to study how thermal noise behaves in non-equilibrium conditions and its impact on GW detectors performance.

Up to now, experiments on thermal noise out of thermodynamic equilibrium involved mainly small-scale systems, as in large-scale ones the fluctuations due to thermal noise become small. Only recently experiments on non-equilibrium macroscopic systems have been performed. Below an example of both is proposed: the study of thermal noise in a silicon micro-cantilever heated by a laser [23] and the RareNoise experiment [22], which studies the effects of breaking energy equipartition on the measurements of temperature in macroscopic oscillators subject to heat flux.

1.4.1 Thermal Noise of a Micro-Cantilever

In his work, Bellon [23] studied the behavior a silicon cantilever heated by partial absorption of light from a laser. The heat was conducted along the cantilever towards the clamped base, creating a significant thermal gradient (see figure 1.11).

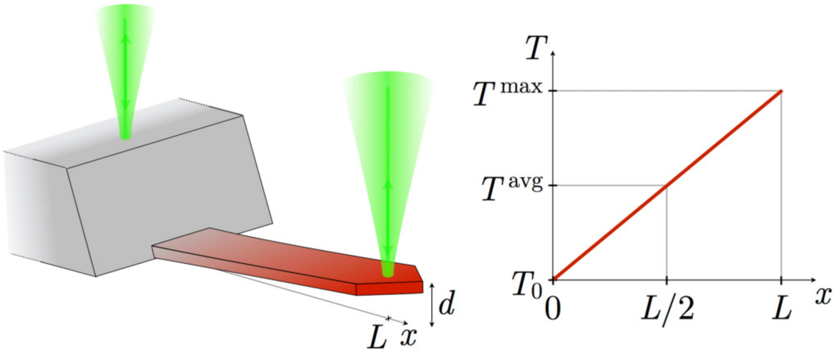

Figure 1.11: Scheme of the experimental setup. The deflection d of a micro-cantilever is measured through the interference of two laser beams, one reflected on the cantilever free end, the other on the clamp holding the cantilever. The sensing beam heats the cantilever and a steady temperature profile driven by the absorbed light power is reached, setting the system in a non-equilibrium steady state (NESS). In a first approximation, the temperature T grows linearly along the cantilever length (i.e. along x). Picture from [23].

The deflection of the cantilever was measured using a differential interferometer, which also acted as the heating source. Sharp resonances in the power spectrum density of the deflection were observed, indicating modes of oscillation assumed to be driven by thermal noise, as can be seen in figure 1.12. The quality factor of these resonances was high, allowing each mode to be modeled as an independent harmonic oscillator.

To quantify the thermal fluctuations of each mode of oscillation n, an effective temperature T_n^{eff} was calculated by extending the equipartition relation, as seen in 1.23:

$$\frac{1}{2}k_n\langle d_n^2\rangle = \frac{1}{2}k_B T_n^{\text{eff}} \tag{1.24}$$

where k_n is the stiffness of the mode, k_B the Boltzmann constant and $\langle d_n^2\rangle$ the mean square deflection of mode n. By tracking then the frequency shift of the resonances with light power, the cantilever temperature profile and average temperature were estimated. The same thing was repeated after adding a tantala coating to the cantilever.

In figure 1.13 are reported the results: the effective temperatures of the first three flexural modes measured on two different cantilevers are plotted as a function of the impinging light power P, and compared it to their average temperature T^{avg} (measured by the resonance frequency shift 1.12). What can be understood from these results is that the behavior of the two cantilevers is very different: for the raw silicon one, T_n^{eff} is mode independent and almost constant close to the room temperature $T_0 = 295$ K. The system therefore shows less fluctuations with respect to the ones expected for a system in equilibrium around its average temperature . For the tantala-coated cantilever instead it can be seen that T_n^{eff} is mode dependent, and it increases with the light power P and results reasonably close to T^{avg} for n $>$ 1. However, the first mode also seems to present a deficit of fluctuations with respect to an equivalent equilibrium situation.

The experiment starts from a generalization of the fluctuation dissipation theorem (FDT) and demonstrates that some non-equilibrium states can lead to unexpectedly low thermal fluctuations,

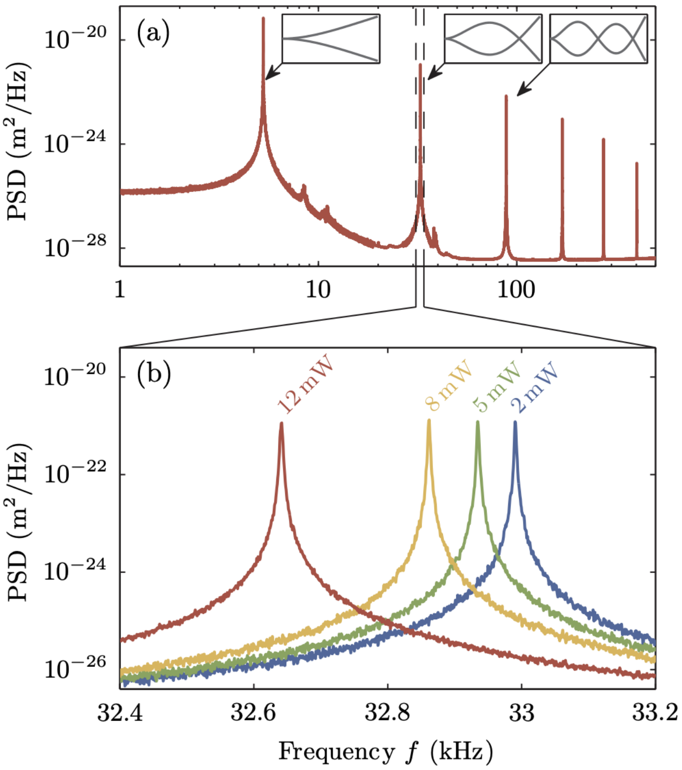

Figure 1.12: PSD of thermal noise induced deflection in vacuum as a function of frequency. (a) Each resonant mode is identified by a sharp peak, associated to the normal mode shape pictured in the insets. The resonances can be modeled as uncoupled simple harmonic oscillators. The area under the PSD curvegives the mean square deflection of each degree of freedom, and defines its effective temperature. (b) With increasing laser power, the cantilever resonance frequencies decrease. Here is shown the case for mode 2. The frequency shift is used to estimate the amplitude of the temperature profile, and thus the average temperature T_{avg}. Picture from [23].

with respect to a system in equilibrium having the same average temperature T^{avg}: therefore spatially inhomogeneous fields of temperature and dissipation mechanisms can lead to an apparent deficit of thermal noise.

1.4.2 The RareNoise Experiment

The RareNoise Experiment [22] aimed to study the behavior of thermal noise fluctuations out of thermodynamic equilibrium, but it differed from Bellon's work by considering macroscopic systems. The research focused on the effect of temperature gradients inevitably present in GW detectors.

The experiment consisted in high precision measurements of the vibrations of a low-loss mechanical oscillator. The measurements were performed both in thermodynamic equilibrium and non-thermodynamic equilibrium steady states (NESS), which were established by imposing a temperature gradient across the oscillator.

These effects were studied in a small frequency range around the oscillator resonance, specifically chosen to fall within the frequency range of interest for GW detectors.

The oscillator consisted in a monolithic aluminum piece, shaped as a cuboid at the end of a square cross-section rod, hosted in a vacuum environment and isolated from external perturbations with a cascade of mechanical filters (for a more detailed description of the setup see chapter 2). In

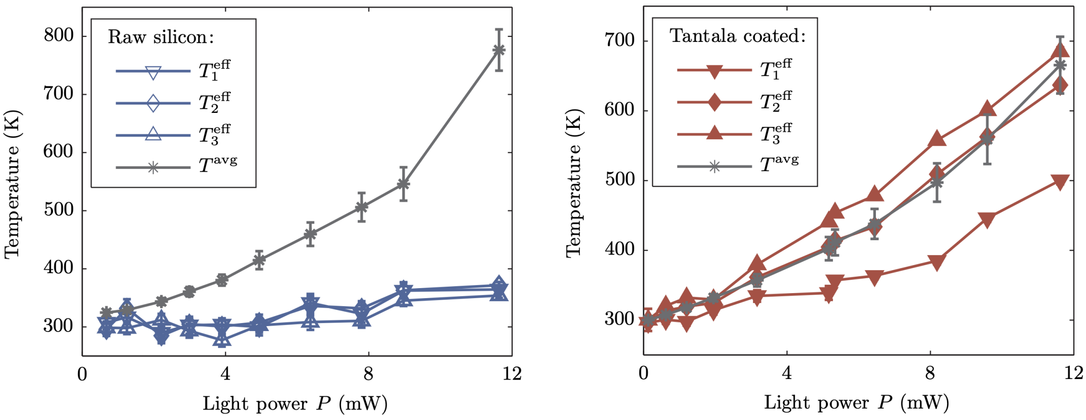

(a) *Silicon cantilever measurements* (b) *Tantala-coated cantilever measurements*

Figure 1.13: Effective temperature T_n^{eff} for the first three flexural modes and average temperature T^{avg} measured for the the silicon (a) and the tantala-coated (b) cantilevers as a function of the impinging light power P. Pictures from [23].

the frequency range where its first transverse and longitudinal modes resonate, respectively ∼320 Hz and ∼1420 Hz (see figure 1.14 (b) and (c)), the dominant noise force acting on the oscillator is of thermal origin [22].

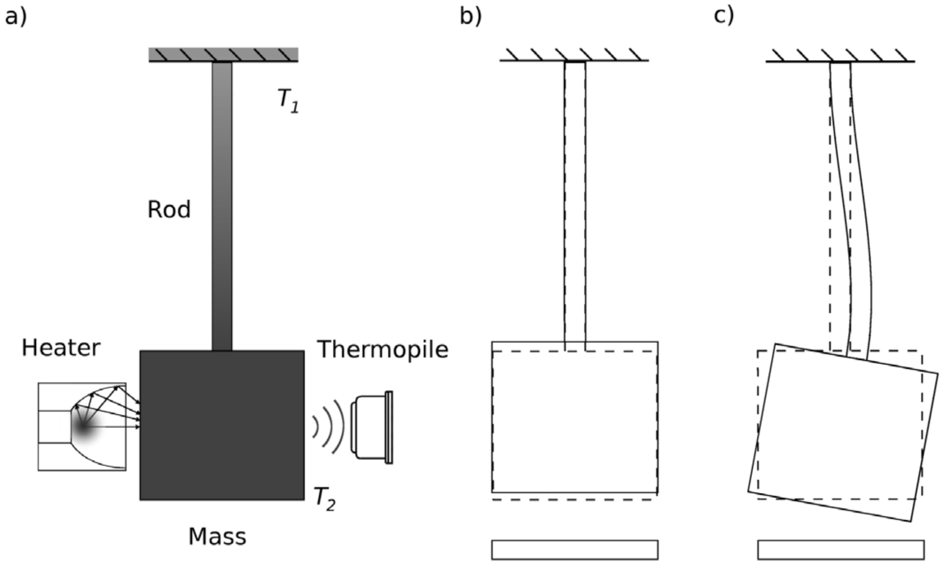

Figure 1.14: Schematic drawing of the resonant oscillator, consisting in a rod with one extreme fixed and the other loaded by a mass free to move. In (a) are visible the contactless thermopile used to read the temperature of the cuboid mass T_2 and the IR heater that heats the cuboid load mass to establish a NESS. A NTC thermometer is used to measure the temperature T_1 on the top of the rod. The temperature profile along the rod in the steady state is shown in gray shading (increasing temperature from light to dark). The first longitudinal mode (b) expected around 1.4 kHz and the first transverse mode (c) around 320 Hz. Picture from [22].

A capacitive readout (see figure 1.15) is used to measure the vibrations of the resonator. The capacitor is formed by a metal plate and the cuboid lower surface.

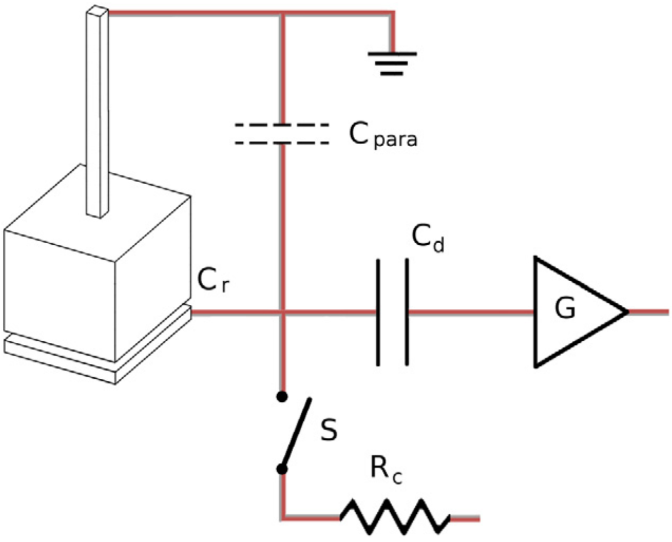

Figure 1.15: Scheme of the capacitive readout used to measure the vibrations of the oscillator. A parallel plate capacitor (C_r) was formed by the bottom surface of the oscillator and a fixed plate; the capacitor was biased to a constant dc voltage through a large resistor (R_c) and then disconnected from it by opening the relay S, which was housed close to the oscillator. Static capacitances in parallel to C_r, represented by the capacitance C_{para} in the picture, had the net effect of reducing the sensitivity of the readout. The signal from the overall parallel capacitor was sent to an amplifier through a C_d decoupling capacitor. Picture from [22].

An infrared heater drives the oscillator out of thermodynamic equilibrium (see figure 1.14 (a)). The temperature is measured on the top of the rod (T_1) and on the cuboid mass (T_2) to detect the induce thermal difference ΔT.

The PSD of the measured vibrations was computed and time averaged. In correspondence of the modes resonances at ∼320 Hz and ∼1420 Hz, peaks are visible in the PSD. A fit of these peaks around the resonance were performed using a Lorentzian curve, which can be considered a good approximation of 1.22 near the resonance:

$$y(f) = \frac{2}{\pi} A \frac{w}{4(f - f_0)^2 + w^2} + y_0 \tag{1.25}$$

where f_0 is the resonance frequency, w the full width at half maximum (FWHM), A the Lorentzian curve area and y_0 the constant used to take into account the additive background noise level (a fit of the longitudinal mode resonance in and out thermodynamic equilibrium is shown in figure 1.16).

The area of the fitted curve A is used as a measurement of the time averaged mean square vibrations $\langle x(t)^2 \rangle$ of the oscillator. In a system in thermodynamic equilibrium, in absence of external noise (as the oscillator is approximated to be), the equipartition law defines a relation between the root-mean-squared vibrations induced by thermal noise and the thermodynamic temperature, so that an effective temperature T_{eff} can be defined, as already seen in 1.23, as:

$$T_{\text{eff}} = \frac{m\omega^2 \langle x(t)^2 \rangle}{k_B} \tag{1.26}$$

where m is the mass of the longitudinal mode that resonates at frequency ω.

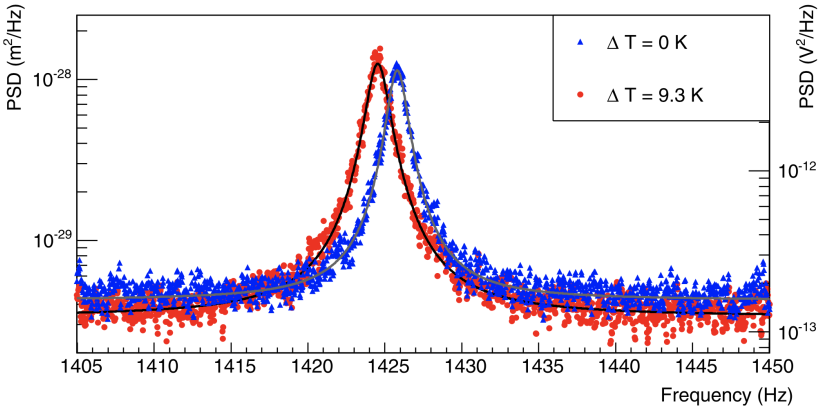

Figure 1.16: Time-averaged PSDs of the amplifier output around the first longitudinal mode in equilibrium (T_{avg} = 288.14 K; blue triangles) and NESS (ΔT = 9.3 K, T_{avg} = 292 K; red circles) The gray line is the fit of the equilibrium PSD, using equation 1.16: $T_{\text{teff}} = [319 \pm 5(stat.) \pm 18(syst.)]$ K. The black line fits the NESS PSD: $T_{\text{teff}} = [402 \pm 6(stat.) \pm 18(syst.)]$ K. Picture from [22].

This measurement, performed in equilibrium at intervals of 25 K around room temperature, confirmed that T_{eff} was a good estimation of the oscillator temperature. Once this has been established, the same measurement was repeated after imposing a NESS by exposing the oscillating mass to heat fluxes. The imposed NESS were characterized by a temperature gradient $\Delta T = T_2 - T_1$ and by an average temperature T_{avg}, calculated as $T_{avg} = (T_1 + T_2)/2$ for the longitudinal mode, while for the transversal mode it was estimated for each mode from the resonance frequency shift, in the same way done by Bellon (figure 1.12). As shown in 1.16, an increase of the PSD around the resonance was observed [22]. To better comprehend the measurements result, the ration $R_{NEQ/EQ} = T_{\text{eff}}/T_{\text{eq}}$, where T_{eq} is the effective temperature at equilibrium, was computed and plotted against the induced temperature gradient ΔT normalized by T_{avg} (figure 1.17).

From 1.17 it can be seen that $R_{NEQ/EQ} > 1$, and in correspondence of the maximum ΔT, $R_{NEQ/EQ} > 1$ by more than four standard deviations. A 4% relative temperature difference seems to be enough to increase the non-equilibrium T_{eff} by 20%, so to raise the effective temperature above the highest physical temperature present across the oscillator, in constrast to what is found by [23]. This result means that in a NESS, T_{eff} is not a valid estimate of the physical temperature anymore, even close to the equilibrium state, and that the energy equipartition principle could be not valid in systems out of thermodynamic equilibrium.

A numerical experiment was conducted in parallel using a 1-dimensional chain of oscillators, the results of which are compatible with the experimental data and are also reported in figure 1.17.

This study questions that the equipartition principle remains valid also out of the thermodynamic equilibrium: it suggests that in presence of a NESS not only the average energy does not match the expected value, but also the energy is not anymore equiparted between the modes, and different modes could be characterized by different temperatures.

The contrasting findings of the two experiments showcased here on the behavior of thermal noise in a NESS induced by a temperature gradient, despite the distinct setups employed, emphasize the necessity of further investigating this subject.

The Non-Equilibrium Thermal Noise experiment, described in chapter 2 and subject of the present work, aims to reproduce the RareNoise experiment results with a different and ideally more sensitive readout system.

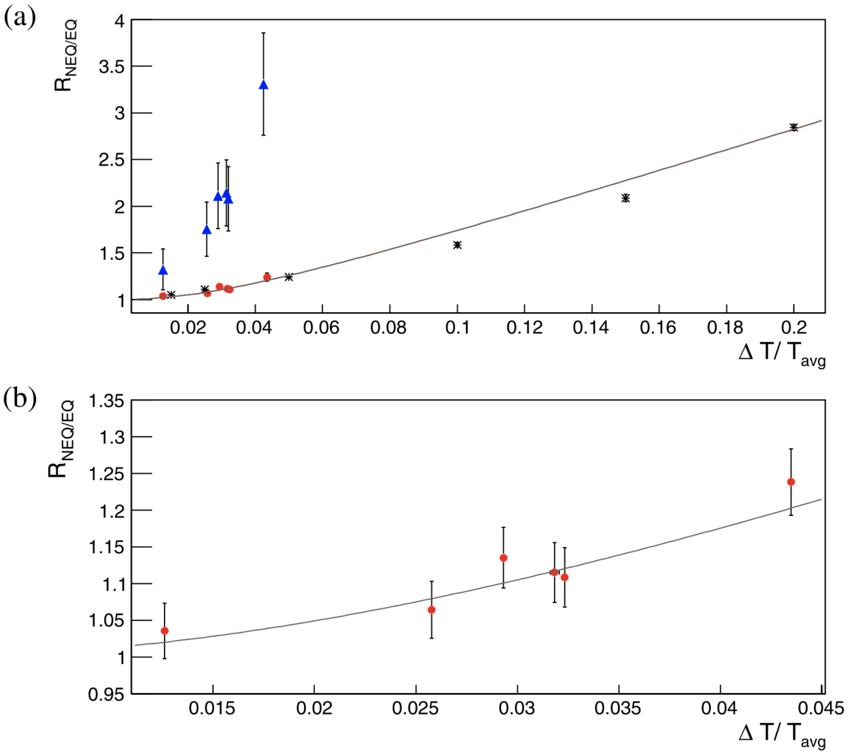

Figure 1.17: (a) Plot $R_{NEQ/EQ}$ for the transverse (blue triangles) and longitudinal (red circles) acoustic modes in NESS against $\Delta T/T_{avg}$. The black stars show the results of the numerical experiment. The gray line is the best fit of the numerical data with the function of equation. (b) Zoom of the results of the longitudinal mode and the line fitting the numerical result in (a). Picture from [22].

Chapter 2

The Non-Equilibrium Thermal Noise Experiment

Section 1.4 provided an overview of the previous works on thermal noise out of thermodynamic equilibrium and of the accomplishments of these studies. The RareNoise experiment, once concluded, provided most of the setup components necessary to install a very similar experiment, which takes the name of Non-Equilibrium Thermal Noise (NETN), described in this work. The NETN experiment is located at the Laboratori Nazionali di Legnaro (Padua) and, as the RareNoise one, aims to study the behavior of thermal noise induced fluctuations in and out of thermodynamic equilibrium, with a substantial difference: the monitoring of the oscillator vibrations, described in the section 1.4.2, no longer takes place via a capacitive readout but via an interferometric readout.

Section 2.1 provides an overview of the NETN experiment, while section 2.2 describes all the components of the experimental apparatus, apart from the interferometric readout, which is described in details along with the data analysis in chapter 3.

2.1 Experiment Overview

The RareNoise experiment provided measurements of thermal noise both in thermodynamic equilibrium and in non-equilibrium steady states (NESS). The latter measured an excess of thermal noise with respect to the one that could be estimated by a simple extension of the fluctuation-dissipation theorem, and also showed a violation of the equipartition of energy (see figure 1.17). This experiment had although some limitations. The measurements were affected by a systematical error, mainly due to the thermal expansion of the aluminum rod and of the cuboid mass which were changing the reference capacity. Furthermore, the calibration of the sensing capacity (see figure 1.15) would not remain constant during the heating transients, making it difficult to accurately estimate them.

The NETN experiment was designed to overcome these difficulties in order to improve the measurements already carried out by the RareNoise one. An interferometric readout, where the oscillating sample surface constitutes one of the reference mirrors, has been implemented in place of the capacitive one for this purpose (see figure 2.1).

The interferometer used to track the mechanical oscillator vibrations is not a simple Michelson but a quadrature phase differential interferometer (QPDI). The two output signals of the implemented QPDI allow to benefit both from the interferometer high sensitivity, and from an unambiguous description of the phase even on multiple fringes. More precisely, two superimposed interferometers are built exploiting two linear polarizations of light, one orthogonal to the other, allowing to measure separately sine and cosine of the optical phase. Combining these two information, the phase can be unambiguously extracted on multiple fringes and used to study the oscillator vibrations due to thermal noise.

One of the main advantages of this readout, with respect to the capacitive one lies in the interferometer "self-calibration": a single fringe corresponds to a $\lambda/2$ displacement and does not require a calibration. For the particular case of a QPDI interferometer, there is also no dependency on the laser power. Thus the interferometric readout is able to track the oscillator vibrations with no systematic errors due to the aluminum thermal expansion, allowing to perform calibrated measurements during the heating transients. A calibration is still always necessary to correct unavoidable imperfections of the system and of the alignment, but, as described in section 3.2, it does not require heating and therefore it does not introduce the systematic errors affecting the RareNoise measurements.

From the QPDI interferometric readout it is then possible to retrieve the optical phase, which encloses information about the oscillator longitudinal vibrations, and therefore on the thermal noise causing them, as described in details in section 3.1.

2.2 Experimental Setup

The NETN experimental apparatus can be seen in figure 2.1, while a scheme of laser optical path through it can be found in figure 3.1.

To integrate the interferometric readout in the RareNoise experiment setup, a compact optical bench has been designed, for it to be screwed in place of the capacitive readout plate (see figure 2.1). As previously said, the oscillating sample is positioned in place of one of the reference mirrors of the interferometer. This allows to track the first longitudinal mode of vibration of the oscillator by studying the optical phase difference between the two laser beams traveling the interferometer arms, and therefore to study the thermal noise causing those vibrations. It is also possible to measure the first transversal mode by cross-correlation, but the latter is not "self-calibrated", as instead happens for the longitudinal mode, as described above. The oscillator is placed in a vacuum chamber equipped with a heater and isolated from external noises by three mechanical filters. These three components are described in the following sections.

Since the interferometer is not a simple Michelson but a QPDI, its readout is measured by a system of four photodiodes, and successively collected by an acquisition system based on a National Instruments PXI platform (see section 2.2.5).

The whole experiment is placed over an mechanically suspended optical bench, where the remaining components needed for the interferometric readout are mounted.

2.2.1 Oscillator

The sample used as a probe to study thermal noise is a monolithic piece of aluminum machined in the shape of a cuboid attached to an upper flange by means of a square cross-section rod. A schematic drawing of the oscillator is visible from fig 2.2 [25].

The mass-rod-suspension sample is machined from a single piece of A15056, a particular aluminum alloy. This material is characterized by low intrinsic mechanical losses, large availability and low cost. In particular its low intrinsic losses motivated its usage in resonant gravitational wave detectors, where the thermal noise associated to losses needed to be minimized.

The cuboid sides are ~5 cm (the precise values can be seen in figure 2.2), with a lower surface polished to be sufficiently reflective for interferometric readout. The rod is 100 mm long with a $(5.5\,mm)^2$ cross-section and is kept along the vertical axis with the mass at the bottom, free to oscillate. On top of the flange, coaxial with the rod, a piezoelectric actuator is mounted, which provides a mean of exciting the oscillator in the vertical direction, and can therefore be used to study the response of the oscillator and test the measuring apparatus.

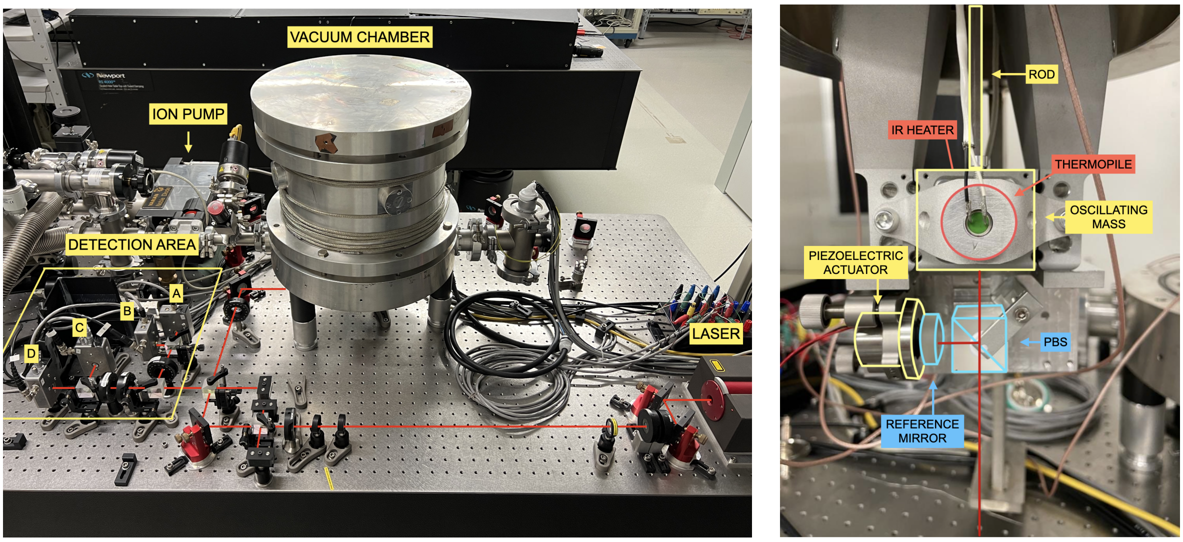

(a) *NETN experimental setup*

(b) *Oscillator inside the vacuum chamber*

Figure 2.1: (a)Photo of the NETN experimental setup located at the Laboratori Nazionali di Legnaro (LNL), Padova. The optical path of the laser beam is highlighted in red: the beam originates in the laser head (lower right), and is then directed by the optical elements towards the vacuum chamber (center of the image). When it enters vertically the vacuum chamber it is divided into the two arms of the interferometer. After the two beams are recombined, the resulting beam exits the chamber and is directed towards the detection area (left), where a beam splitter divides it and directs it towards the four photodiodes (A, B, C, D), which will read and collect the resulting signal. (b) Photo of the flange housing the interferometer; this is constitued by the oscillator, a reference mirror (provided with a piezoelectric actuator) and a PBS that divides and recombines the beams, after they have been reflected one by the reference mirror and the other by the lower oscillator surface. A thermopile is positioned on the front of the oscillating mass, while a IR heater is positioned on the back (thus is not visible in the photo). The beam optical path is highlighted in red.

The oscillator modes of interest are the first longitudinal one, resonating at about 1.4 kHz (fig 2.2 (b)), and the first transverse one, resonating around 300 Hz (fig 2.2 (c)), since they are the easiest to measure and the ones for which thermal noise induces the larger vibrations. In its first longitudinal mode of vibration, the aluminum oscillator can be seen as a spring-mass system with the rod acting as the spring and the cuboid as the mass attached to one of its ends. The system dynamics therefore is that of a damped harmonic oscillator, and thermal noise acts as a stochastic force on it (see section 1.4.2).

2.2.2 Heater

In order to produce a temperature gradient across the oscillator and establish a NESS, an infrared heater is installed to face one side of the cuboid mass. The IR heater functions as a 3.6 Ω resistor that generates heat through the Joule effect, emitting radiation as a black-body with a power determined by the current flow. The resistor is positioned at the focal point of a parabolic mirror, which directs all radiation emitted by the resistor towards the cuboid mass of the oscillator (see figure 1.14 (a)).

When the oscillating mass is heated by the resistor a temperature gradient ΔT between the top

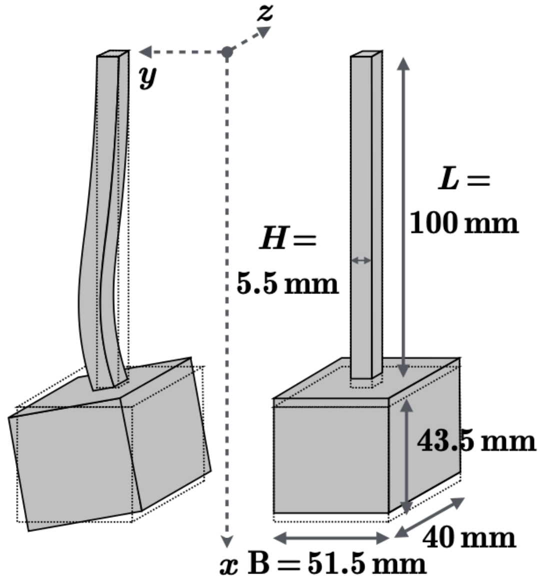

Figure 2.2: Schematic drawing of the oscillator: it consists in a monolithic piece of aluminum machined in the shape of a cuboid and attached to an upper flange by means of a square cross-section rod of length $L = 100\,mm$ and square cross section $H^2 = (5.5\,mm)^2$. The cuboid side is roughly $B = 50\,mm$. In the picture the two motions of the oscillator are depicted, the first transverse mode (left) and the first longitudinal one (right). Picture from [25].

(T_1) and the bottom (T_2) of rod is created, establishing a NESS.

To measure the temperature of the upper end of the rod and of the cuboid mass, an NTC thermistor mounted on a copper plate at the base of the rod and a thermopile facing the other side of the cuboid mass with respect to the heater are used, respectively. The thermopile provides also a measure of the ambient temperature inside the vacuum chamber. The ambient temperature outside the vacuum chamber (temperature inside the laboratory) is monitored by a thermometer.

2.2.3 Mechanical Suspensions

The setup is placed on an air suspended optical table. The residual environmental mechanical noise is reduced by using a three-stage mechanical filter. The NETN experiment reuses the three-stage mechanical filter developed in the past as suspension prototype for the RareNoise experiment [21], where it was designed to fit in the volume of the vacuum chamber (described in section 2.2.4). Each of the three stages have diameter 305 mm, height 260 mm and a mass of 17.4, 17.4, and 19.8 kg respectively, from bottom to top. The third one is more massive with respect to the previous two since it must support a 6.6 kg payload, consisting of a flange for housing the oscillator-reference mirror-PBS assembly. A scheme and a picture of the mechanical suspensions design can be seen in figure 2.3.

A passive mechanical filter consists of a mechanical oscillator that resonates at a frequency ν_0 much lower than the frequencies of interest, in the NETN case lower than $\sim 300Hz$, the frequency of the first transverse mode of the oscillator.

For frequencies ν much higher than the resonance frequency of the filter ν_0 and in a low-loss regime where $\nu_0 \ll \nu \ll \nu_0/\phi$, with ϕ being the loss angle of the oscillator represented by the mechanical filter, an input vibration is depressed at the output by a factor defined by the transfer

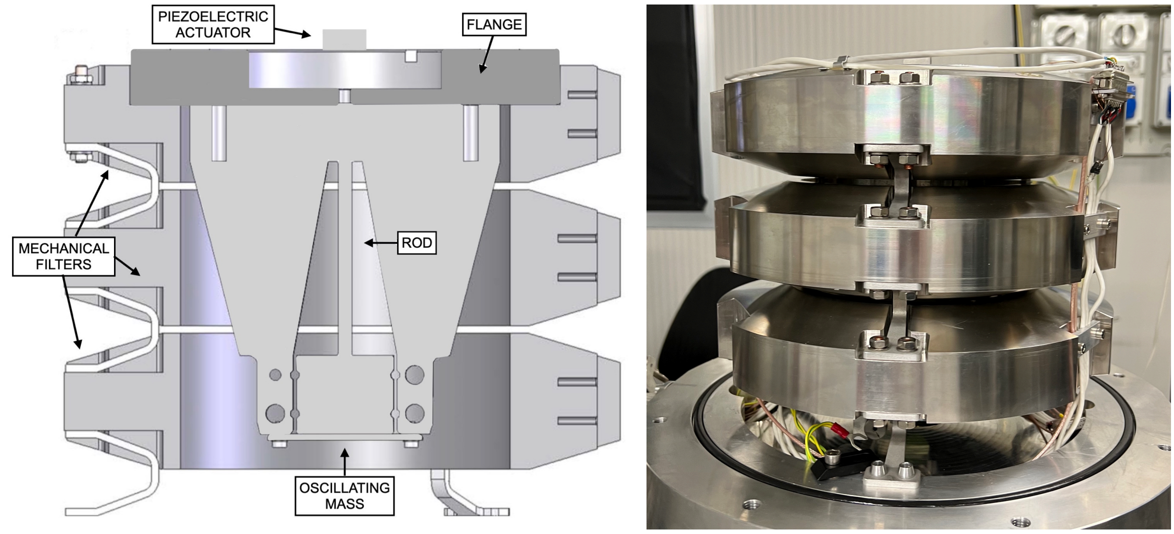

(a) *Scheme of the mechanical suspensions design* (b) *Picture of the mechanical suspensions*

Figure 2.3: (a) Cross section of the full assembly with the payload. The oscillator inserted co-axially inside the mechanical filters is visible. Also the piezoelectric actuator is visible, positioned over the top flange. Picture from [21]. (b) Picture of the full assembly of the suspension with payload. The picture shows also the white cables connecting the thermopiles, thermometers and heater. On top of the system the piezoelectric actuator used to estimate the oscillator tranfer function is visible.

function [21]:

$$T(\nu_0, \nu) = \frac{\nu_0^2}{\nu_0^2 - \nu^2} \tag{2.1}$$

When N filters are positioned in cascade, the total transfer function is the product of the individual transfer functions and, for high enough frequencies, it shows an isolation that goes as ν^{2N}. The three filters implemented in the NETN setup are designed to work in the frequency range 300-2000 Hz. Above 2000 Hz the mechanical filters lower acoustic mode resonate, therefore they stop to behave as rigid bodies and exhibit internal modes of vibration. The internal resonances of the mechanical structure cause the transfer function to display a pattern of resonances in the high-frequency region (above 2000 Hz), thus worsening the suspension performance.

The resonance frequency of a single stage is $\nu_0 \approx$38 Hz, while the overall cascade of filters shows a more complicated behavior. The measured vertical transfer function of the whole suspension system is reported in figure 2.4.

The vacuum chamber (containing filters and payload) is positioned on three nylon spacers, which in turn are sustained by three aluminum cylinders, and the overall system lies on the optical bench. The nylon spacers are inherited from the RareNoise experiment, in which they were used as thermal insulators, while the aluminum ones have been integrated in the NETN experiment to raise the vacuum chamber. In order to isolate even more the oscillator from external vibrations, between each of the three nylon supports and the corresponding metallic cylinder is placed a cube of Sylodamp, a vibration damping elastomer, which acts as a mechanical filter. The vacuum chamber spacers and the Sylodamp placed on them are visible in figure 2.5. This material allows in particular to reduce the vibrations in correspondence of the resonances in the range $10 \div 70$ Hz (which propagate even above 100 Hz through the higher harmonics of these modes) shown in figure 2.4.

A large piece of Sylodamp is also placed between the optical bench and the ion pump that

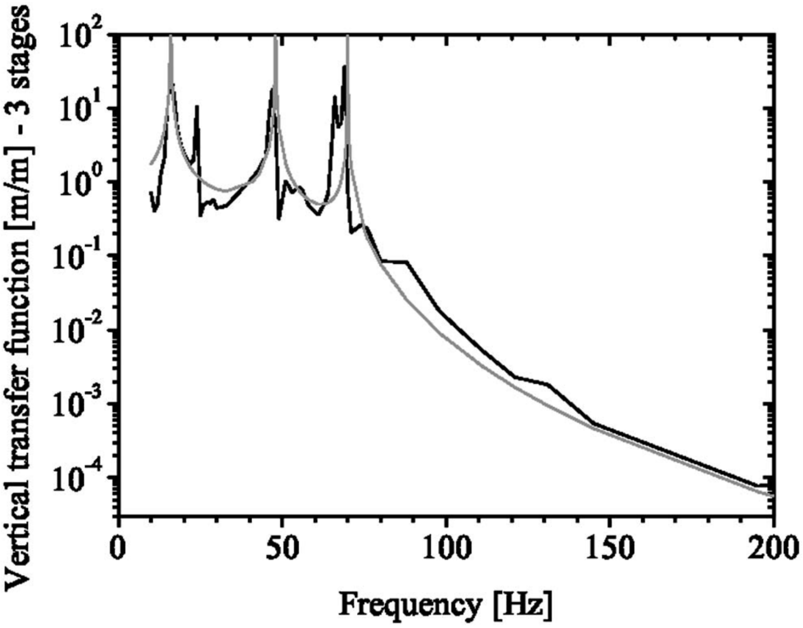

Figure 2.4: Vertical Transfer function of the mechanical filter. The black line is the experimentally measured transfer function. The gray line is the prediction from the coupling in cascade of the three stages, which are three oscillators of masses, respectively, 17.4, 17.4, and 19.8 kg, each resonating at the frequency $\nu_0 \approx 38Hz$. Picture from [21].

rests over it; being rigidly connected to the vacuum chamber, the pump would otherwise allow the vibrations to reach the chamber bypassing the isolation of the legs.

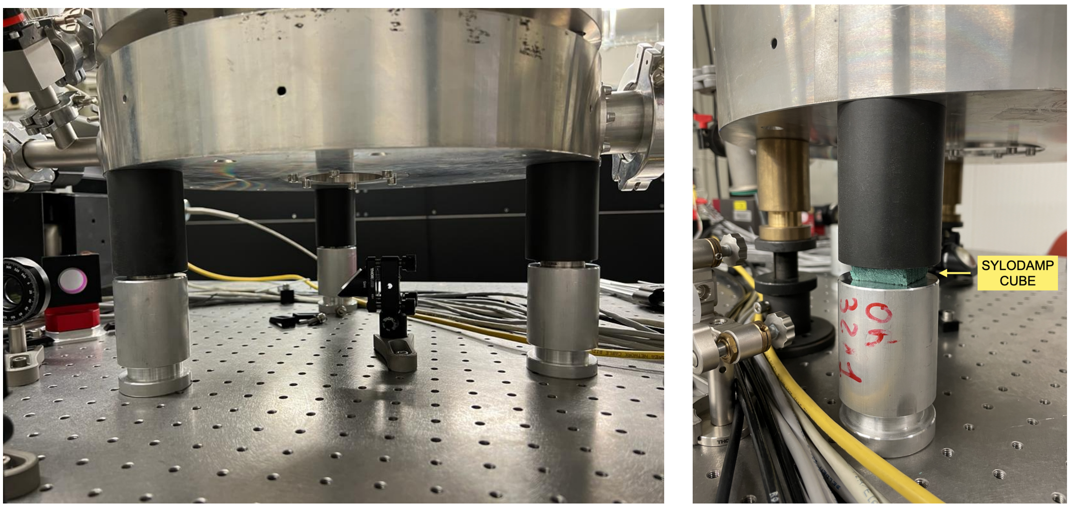

(a) *Pillars sustaining the vacuum chamber*

(b) *Sylodamp positioned inside the pillars*

Figure 2.5: (a) Photo of the three pillars sustaining the vacuum chamber, consisting of a nylon part (black) and an aluminum one (b) One of the three pillars sustaining the vacuum chamber; between the nylon (back) and the aluminum supports, the cube of damping material called Sylodamp (green) is placed in order to minimize the transmission of external vibration to the chamber.

2.2.4 Vacuum System

In order to reduce external disturbancies to both the oscillator and the readout system, including the acoustic noise caused by sound waves propagation in air and externally induced thermal effects, the oscillator and the three mechanical filters surrounding it are kept inside a vacuum chamber.

The vacuum chamber is a prototype of the one used in the past for the RareNoise experiment [21] and consists of two aluminum blank flanges, with a 400 mm diameter, acting as base and top of the box, spaced by an aluminum tube of internal diameter 305 mm and height 260 mm. A glass window has been added on the chamber base to let the laser beam enter and exit during the measurements. The vacuum chamber can be seen in figure 2.1 (a).

The vacuum system consists of three pumping stages (displaced as shown in figure 2.7): a dry scroll pump, a turbo-molecular pump (figure 2.8 (a)), and an ion-pump (figure 2.8 (b)).

The scroll pump is used to create a pre-vacuum ($\sim 10^{-1}$ mbar), then the turbo-molecular pump, working in parallel with the scroll, reaches a pressure of the order of $10^{-5}/10^{-6}$ mbar. This level of vacuum would be sufficient for the experiment, but the turbo-molecular pump vibrations induces a high mechanical noise on the optical table. Therefore, the combination of the scroll and the turbo-molecular pumps is used only to pre-evacuate the chamber, in order to successively turn on the ion pump. During the measurements the ion pump is left alone pumping into the chamber, where it maintains a pressure of the order of 10^{-6} mbar. Figure 2.6 shows the trend of the pressure inside the vacuum chamber during the procedure described above. Each step of the procedure is indicated by specifying which pumps are acting on the system.

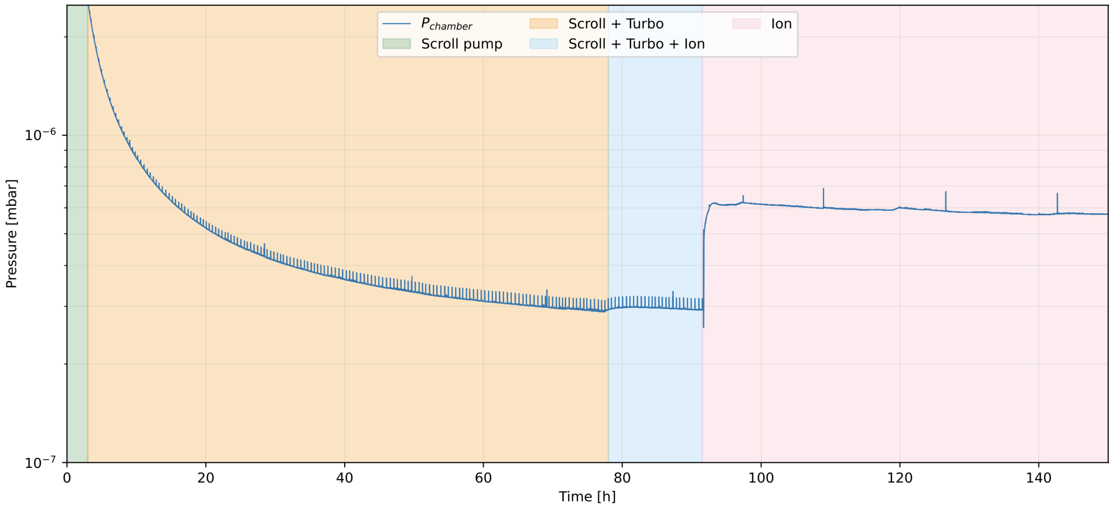

Figure 2.6: Trend of the pressure inside the vacuum chamber during the procedure of establishing the vacuum. Each step of the procedure is distinguished by a different color.

Three vacuum valves are placed as can be seen in figure 2.7. Three vacuum gauges are used to measure the pressure in the chamber, at the head of the ion pump and at the head of the turbo-molecular pump (respectively gauge 1, 2 and 3 in the scheme 2.7).

2.2.5 Data Acquisition

The four photodiodes outputs are acquired using a 24-bit resolution ADC NI PXI-4462 DAQ board, with a sampling frequency $f_{fast} = 8$ kHz in a ± 10 V range (fast channels).

All the enviromental parameters are acquired with a sampling frequency $f_{slow} = 1$ Hz by NI 9219 24-bit universal analog inputs (slow channels). The monitored environmental parameters are the temperatures measured by the NTC thermistor at the base of the rod and by the thermopile

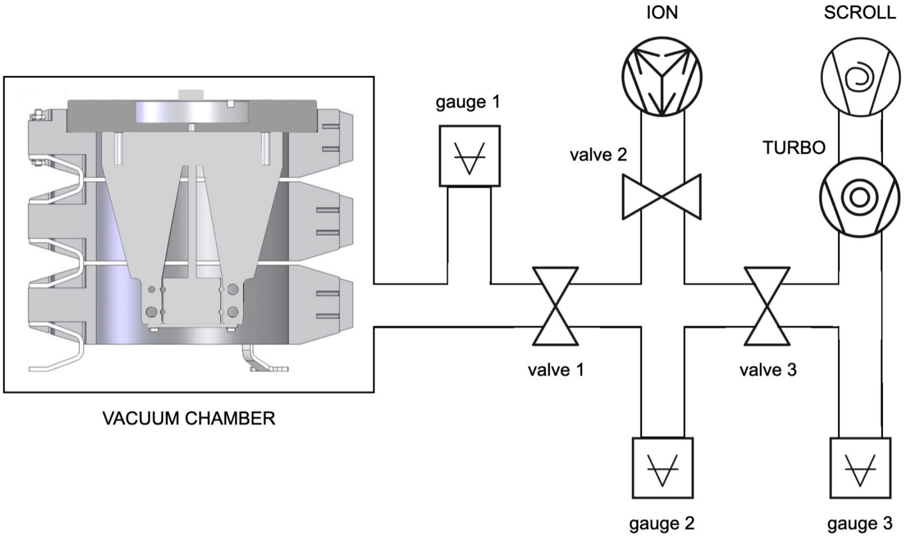

Figure 2.7: Scheme of the vacuum system. The three pressure gauges and the three valves allow to monitor and control the system. The turbo molecular pump and the scroll pump are used to reach the pressure in the chamber of $10^{-5}/10^{-6}$ mbar. Once that level of vacuum is reached, the ion pump is turned on and used to maintain a pressure of the order of 10^{-6} mbar. During the measurements, turbo-molecular and scroll pump are turned off and detached one from the other, to minimize the vibrations transmitted to the experimental apparatus.

facing the cuboid mass (T_1 and T_2), the ambient temperature, measured both inside and outside the vacuum chamber, along with the pressures monitored by the vacuum gauges placed on the setup.

The acquisition system is based on a National Instruments PXI platform. The data acquisition software, which is developed using NI LabView, allows both a real-time visualization of data from fast and slow channel and their storage into files. The sampled fast channel data are stored in series of 20 minutes long BIN files and the data analysis is carried out offline with custom Python scripts and functions.

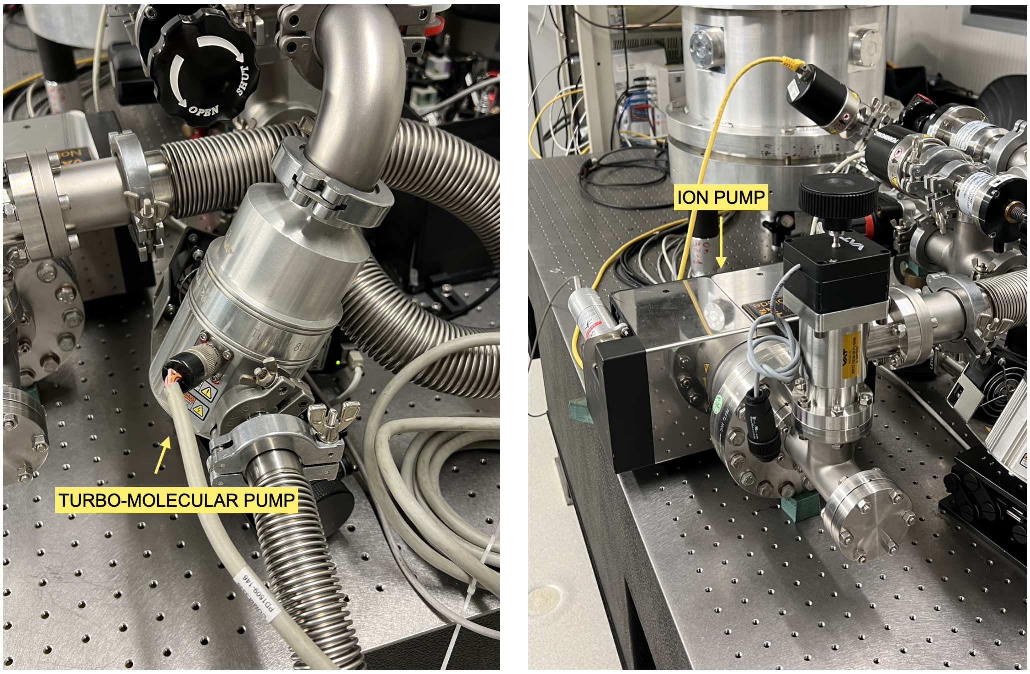

(a) *Turbo-molecular pump* (b) *Ion pump*

Figure 2.8: (a) Photo of the turbo-molecular pump used, after the accension of the scroll pump and in combination of it, to lower the pressure enough to turn on the ion pump ($\sim 10^{-5}$ mbar). Once the ion pump is able to pump alone in the chamber, the turbo-molecular pump is turned off and disconnected from the scroll pump, to avoid the transmission of ground vibrations to the table. (b) Photo of the ion pump used to generate and maintain the vacuum inside the vacuum chamber. The green piece of Sylodamp material, used to prevent the transmission of ground vibrations to the system, is visible under the pump.

Chapter 3

Interferometric Readout and Data Analysis

Chapter 2 was dedicated to the detailed description of the experimental setup. It has been seen that the latter is designed to perform high precision measurements of the vibrations induced longitudinally in a mechanical oscillator by thermal noise, both in and out of thermodynamic equilibrium. In this chapter the focus is on the interferometric readout of the oscillator vibrations. Section 3.1 describes the optical layout and analyzes the interferometer output assuming ideal optical components. Section 3.2 discusses the limits of the experimental case with respect to the ideal one and describes the procedure of readout calibration performed using the photodiodes outputs. Section 3.3 describes how the spectral analysis on the interferometric readout is carried out. This analysis allows to extract, from the photodiodes output, information on the oscillator vibrations and to measure therefore the thermal noise affecting the oscillator.

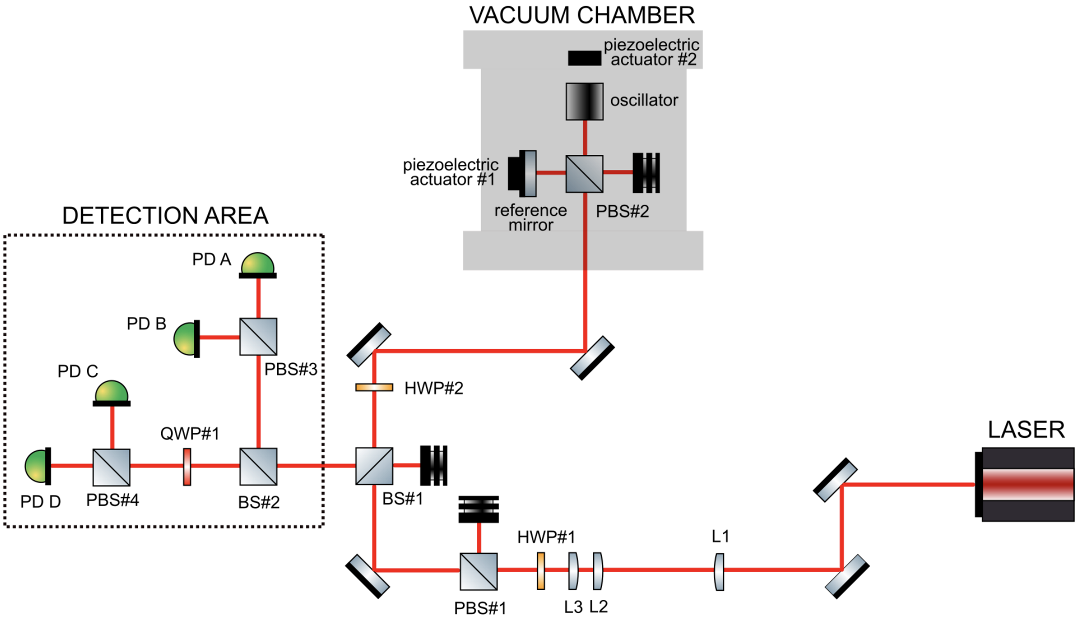

Figure 3.1: Schematized optical setup. The label *detection area* refers to the area containing the four photodiodes collecting the quadrature signals.

3.1 Ideal Case

A scheme of the interferometer setup is shown in figure 3.1, where all the optical elements that the beam encounters are indicated. From now on, as can be seen from the scheme, the area including the four photodiodes that collect the quadrature signals is referred to as the *detection area.*

The laser source emits a 1064 nm wavelength, linearly polarized beam. A telescope consisting of three lenses (L1, L2, L3), with focal length respectively 100, 150 and 1000 mm, is used to collimate the beam. The produced beam is characterized by a beam waist of ∼1 mm and a raylight range of ∼2.95 m.

The combination of a half-wave plate (HWP#1) and a polarizing beam splitter (PBS#1) is used as a power controller, allowing to have in transmission a p-polarized beam with adjustable power, while the s-polarization is reflected and absorbed by a damper. The power tuning is possible through the rotation of the half-wave plate angle and allows to adjust the power reaching the photodiodes to the right amount, which is enough to use the full dynamic range of the ADC boards without saturating the photodiodes.

In order to calculate the intensity reaching the four photodiodes, at the output of the phase quadrature interferometer, Jones formalism is adopted: the beam is described by its Jones vector, where the first component represents the p-polarized beam and the second component the s-polarized one, while each optical element present in the setup is described by its Jones matrix. The Jones matrix of optical elements relevant for the setup is reported in table 3.1. The interaction with an optical element is performed by multiplying the beam Jones vector with Jones matrix of the optical element, indicated using the symbols reported in table 3.1. Vectors are distinguished from scalars graphically by the use of bold text.

Optical component	Symbol	Jones Matrix
HWP(22.5°)	$\mathbb{J}_{\frac{\lambda}{2}}$	$\frac{1}{\sqrt{2}}\begin{pmatrix}1 & 1\\1 & -1\end{pmatrix}$
HWP(−22.5°)	$\mathbb{J}_{-\frac{\lambda}{2}}$	$\frac{1}{\sqrt{2}}\begin{pmatrix}1 & -1\\-1 & -1\end{pmatrix}$
QWP(45°)	$\mathbb{J}_{\frac{\lambda}{4}}$	$\frac{1}{\sqrt{2}}\begin{pmatrix}1 & i\\i & 1\end{pmatrix}$
PBS$_t$	$\mathbb{J}_{PBS_t}$	$\begin{pmatrix}1 & 0\\0 & 0\end{pmatrix}$
PBS$_r$	$\mathbb{J}_{PBS_s}$	$\begin{pmatrix}0 & 0\\0 & 1\end{pmatrix}$
Beam Splitter	$\mathbb{J}_{BS}$	$\frac{1}{\sqrt{2}}\begin{pmatrix}1 & 0\\0 & 1\end{pmatrix}$
Mirror	$\mathbb{J}_{M}$	$\begin{pmatrix}1 & 0\\0 & -1\end{pmatrix}$

Table 3.1: List of the Jones matrices of the optical components present in the setup and interacting with the laser beam. For each Jones matrix is indicated the symbol used in the text to refer to it.

After PBS#1, the field can be described as:

$$\boldsymbol{E_0} = \mathbb{J}_{PBS_t}\boldsymbol{E_{in}} = E_{in}\begin{pmatrix}1\\0\end{pmatrix} \tag{3.1}$$

where E_{in} describes the Gaussian beam entering the setup after traversing the HWP.

The first element it then encounters is a 50:50 beam splitter (BS#1), which directs half of the beam power towards the chamber area, while the other half is absorbed by a damper. Then an half-wave plate (HWP#2), with the fast axis set at an angle of 22.5°, rotates the beam polarization in order to equally divide it in p and s-polarization. Therefore the beam that enters the vacuum chamber area can be described as:

$$\boldsymbol{E_{chamber}} = \mathbb{J}_{\frac{\lambda}{2}}\mathbb{J}_{BS}\boldsymbol{E_0} = \frac{E_{in}}{2}\begin{pmatrix} 1 \\ 1 \end{pmatrix} \tag{3.2}$$

The beam goes through a window to enter the vacuum chamber. Inside the chamber it encounters PBS#2, which divides the two polarizations: the p-polarization is transmitted towards the lower surface of the oscillator, that is used as the moving mirror of the Michelson interferometer, while the s-polarization is reflected towards the reference mirror of the interferometer.

The beam transmitted by the PBS and reflected by the oscillator is described as:

$$\boldsymbol{E_O} = \mathbb{J}_M\mathbb{J}_{PBS_t}\boldsymbol{E_{chamber}} = \frac{E_{in}}{2}e^{i2k(L_O+\delta x)}\begin{pmatrix} 1 \\ 0 \end{pmatrix} \tag{3.3}$$

where $k = \frac{2\pi}{\lambda}$ is the beam wave number, L_O is the distance covered by the light going from the PBS to the oscillator and back and δx the oscillator displacement.

The beam reflected by the PBS and reflected again by the reference mirror is described as:

$$\boldsymbol{E_M} = \mathbb{J}_M\mathbb{J}_{PBS_r}\boldsymbol{E_{chamber}} = \frac{E_{in}}{2}e^{i2kL_M}\begin{pmatrix} 0 \\ -1 \end{pmatrix} \tag{3.4}$$

where the distance covered by the light, going from the PBD to the reference mirror and back, in this case is denoted L_M. The two beams then recombine at the PBS, so that at the exit of the chamber the total beam is:

$$\boldsymbol{E_{recombined}} = \boldsymbol{E_O} + \boldsymbol{E_M} = \frac{E_{in}}{2}\begin{pmatrix} 1 \\ -e^{i\psi} \end{pmatrix} \tag{3.5}$$

where $\psi = 2k(L_M - L_O - \delta x) = 2k(\Delta L - \delta x)$. After the recombination, and before entering the detection area, the beam passes a second time through HWP#2, that in this case is equivalent to an half-wave plate set at $-22.5°$. Then it reaches again BS#1, where half of the power is transmitted and absorbed by a damper, while half is reflected into the detection area. The beam that enters the detection area is therefore described as:

$$\boldsymbol{E_{detection}} = \mathbb{J}_{BS}\mathbb{J}_{-\frac{\lambda}{2}}\boldsymbol{E_{recombined}} = \frac{E_{in}}{4}\begin{pmatrix} 1 + e^{i\psi} \\ -1 + e^{i\psi} \end{pmatrix} \tag{3.6}$$

Inside the detection area BS#2 divides the beam between the two analysis arms of the QPDI. The beam reaching PBS#3 can be described as:

$$\boldsymbol{E_{AB}} = \mathbb{J}_{BS}\boldsymbol{E_{detection}} = \frac{E_{in}}{\sqrt{32}}\begin{pmatrix} 1 + e^{i\psi} \\ -1 + e^{i\psi} \end{pmatrix} \tag{3.7}$$

The beam in the arm AB is then splitted by PBS#3, which transmits the p-polarization towards the photodiode A and reflects the s-polarization towards the photodiode B. The beams reaching the two photodiodes A and B are therefore described as:

$$\boldsymbol{E_A} = \mathbb{J}_{PBS_t}\boldsymbol{E_{AB}} = \frac{E_{in}}{\sqrt{32}}\begin{pmatrix} 1+e^{i\psi} \\ 0 \end{pmatrix} \tag{3.8}$$

$$\boldsymbol{E_B} = \mathbb{J}_{PBS_r}\boldsymbol{E_{AB}} = \frac{E_{in}}{\sqrt{32}}\begin{pmatrix} 0 \\ -1+e^{i\psi} \end{pmatrix} \tag{3.9}$$

In the CD arm the beam first passes through a quarter-wave plate with the fast axis set at an angle of 45° (QWP#1), before reaching the polarizing beam splitter (PBS#4). QWP#1 causes a $\frac{\pi}{2}$ phase shift on the C and D signals with respect to the A and B ones. This phase shift generates quadrature signals that, as described in the previous chapter, allow to unambiguously extract the optical phase ψ by measuring both its sine and cosine. The beam in the CD arm arriving to PBS#4 can be described as:

$$\boldsymbol{E_{CD}} = \mathbb{J}_{\frac{\lambda}{4}}\mathbb{J}_{BS}\boldsymbol{E_{detection}} = \frac{E_{in}}{8}\begin{pmatrix} 1+e^{i\psi}-i+ie^{i\psi} \\ -1+e^{i\psi}+i+ie^{i\psi} \end{pmatrix} \tag{3.10}$$

After QWP#1, PBS#4 splits and directs the two polarizations towards the photodiodes C and D, in the same dynamics of the AB arm. The beam seen by the photodiodes C and D is described as:

$$\boldsymbol{E_C} = \mathbb{J}_{PBS_r}\boldsymbol{E_{CD}} = \frac{E_{in}}{8}\begin{pmatrix} 0 \\ -1+e^{i\psi}+i+ie^{i\psi} \end{pmatrix} \tag{3.11}$$

$$\boldsymbol{E_D} = \mathbb{J}_{PBS_t}\boldsymbol{E_{CD}} = \frac{E_{in}}{8}\begin{pmatrix} 1+e^{i\psi}-i+ie^{i\psi} \\ 0 \end{pmatrix} \tag{3.12}$$

For each photodiode the incident power P is proportional to the beam intensity $I = |EE^*|$ and results to be:

$$P_A = \frac{P_{in}}{16}(1+cos\psi) \qquad P_B = \frac{P_{in}}{16}(1-cos\psi) \tag{3.13}$$

$$P_C = \frac{P_{in}}{16}(1+sin\psi) \qquad P_D = \frac{P_{in}}{16}(1-sin\psi) \tag{3.14}$$

Combining the signals read by the two pairs of photodiodes, A and B, C and D, the phase can be unambiguously extracted. Combining therefore the relations 3.13 and 3.14, the cosine and the sine of ψ are given by:

$$cos\psi = \frac{P_A - P_B}{P_A + P_B} \equiv C_x \tag{3.15}$$

$$sin\psi = \frac{P_C - P_D}{P_C + P_D} \equiv C_y \tag{3.16}$$

where C_x and C_y are called the "contrasts" of the two couples of photodiodes. Once $cos\psi$ and $sin\psi$ are known, the phase is retrieved by using the four quadrant arctangent, a function that assumes values included in a continuous interval of modulus 2π.

In relations 3.15 and 3.16, the term P_{in} contained in the powers measured by the photodiodes simplifies, and therefore the contrasts are independent of the power of the laser entering the setup and of its fluctuations.

Also, in this ideal case, the visibility of each photodiode is:

$$\mathcal{V} = \frac{P_{max} - P_{min}}{P_{max} + P_{min}} = 1 \tag{3.17}$$

The advantage of using a QPDI is even more evident defining the complex contrast C:

$$C \equiv C_x + iC_y = e^{i\psi} \tag{3.18}$$

The unambiguous extraction of ψ is clear when displaying the contrast C in the complex plane: it describes a circle with unitary radius centered in (0,0). Therefore, one measurement of the optical phase ψ correspond to a polar angle in this plane.

The optical phase ψ can be expressed as:

$$\psi = 2k(L_M - L_O - \delta x) = \frac{4\pi}{\lambda}(\Delta L - \delta x) \tag{3.19}$$

where two contributions can be distinguished: ΔL, the intrinsic optical path difference between the two interferometer arms, which may vary slowly with thermal drifts, and δx, the mechanical oscillator displacement, which can be seen as an oscillation around the mean value of ΔL. Since the two contributions are summed in 3.19, the sensitivity of the contrast C with respect to δx does not depend on ΔL:

$$\left| \frac{dC}{d(\delta x)} \right| = \frac{4\pi}{\lambda} \tag{3.20}$$

Thus the working point (the position on the interference fringe, corresponding to the position on the unitary circle) does not need to be optimized, since the sensitivity is unaffected by it. This is particularly advantageous since, during the measurement, the working point can experience some drifts, due for example to the temperature changing: being the sensitivity unaffected by it, the measured displacement remains calibrated. Once the optical phase is determined, the oscillator displacement is obtained as:

$$\delta x = \frac{\lambda}{4\pi}\psi \tag{3.21}$$

3.2 Real Case

What was described in the previous section was an ideal case, which does not consider the inevitable losses in the optical elements and the deviation of their optical properties from the nominal ones. The reflectivity of the mirrors is for example not exactly unitary and has a slight different behavior for the s and p-polarizations, as well as the beam splitter does not reflect exactly

50% of the beam and transmit the other 50%, or the polarizing beam splitter does not transmit and reflect perfectly the p and s-polarizations respectively, but partially reflects the p and transmits the s-polarization. Each element of the setup contributes, along with a possible misalignment of the optical setup, to make formulas 3.13 and 3.14 not exactly valid. In particular, the visibility 3.17 of the power measured by each photodiode is lower than the unitary value. Moreover, in the ideal case a plot of the two contrasts C_y and C_x in the complex plane, at the variation of ψ, would result in a circle of unitary radius, with ψ the polar angle. In the real case instead it results in something closer to an ellipse.

3.2.1 Calibration

In order to account for the imperfections of the instrument and of the alignment, the Heydemann's correction is performed [18]: the closed curve in the (C_x, C_y) plane obtained in the real case, corresponding to an excursion of ψ of at least 2π, represents the calibration curve. This curve is approximated by an ellipse and fitted to obtain the parameters necessary to calibrate the system. This calibration makes it possible to correctly translate the measured contrast into a displacement of the mechanical oscillator.

The calibration curve is constructed experimentally by acquiring for a few seconds the power collected by the four photodiodes, while the working point is scanned. The scanning of the working point is performed by feeding the piezoelectric actuator attached to the reference mirror with a sinusoidal voltage signal, at an angular frequency ω, thus varying the lenght L_M.

This allows to explore the full $[0,2\pi]$ range of phases, and so to sweep at least one entire interference fringe. The power collected, stored into a calibration file, is used to compute the contrasts C_x and C_y at the variation of the working point, and therefore at the variation of ψ, using the equations 3.15 and 3.16. The closed curve in the (C_x, C_y) plane is then fitted by the parametric equations of an ellipse:

$$C_x = X_0 + X cos(\psi) \tag{3.22}$$

$$C_y = Y_0 + Y sin(\psi + \phi) \tag{3.23}$$

Where X_0 and Y_0 represent the coordinates of the ellipse center, X, Y the projection of the semi axes on the x and y directions and ϕ its precession. Once these five parameters are obtained from the fit, equations 3.22 and 3.23 can be used to retrieve the optical phase ψ and thus the displacement δx:

$$cos(\psi) = \frac{C_x - X_0}{X} \tag{3.24}$$

$$sin(\psi) = \frac{C_y - Y_0}{Y cos(\phi)} - \frac{C_x - X_0}{X} tan(\phi) \tag{3.25}$$

An example of calibration is shown in figure 3.2.

Once the values of $cos\psi$ and $sin\psi$ are obtained from 3.24 and 3.25, they can be used, to obtain the value of the optical phase difference ψ.

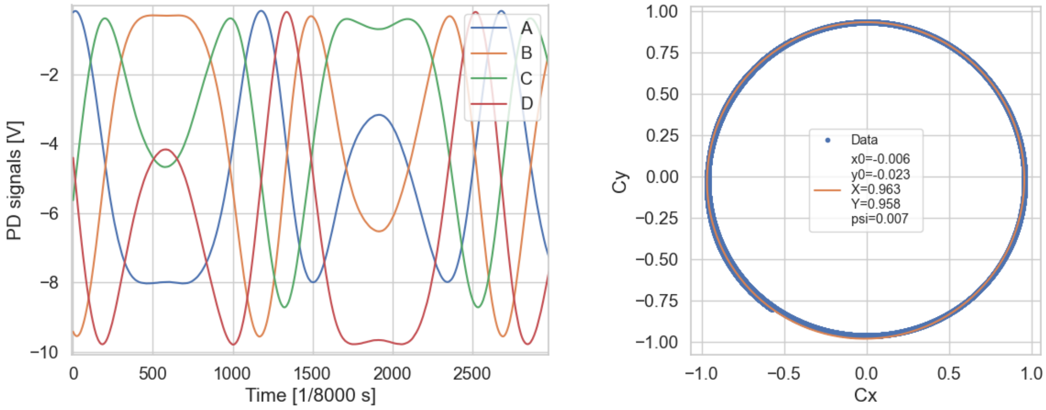

(a) *Photodiodes signal during calibration*

(b) *Calibration curve*

Figure 3.2: Example of calibration via piezoelectric excitation. (a) Outputs of the four photodiodes during the excitation of the piezoelectric actuator on the reference mirror with a sinusoidal voltage of amplitude 2 Vpp, offset 1 V and frequency 3 Hz. (b) Constrasts C_x and C_y (blue data) obtained from the photodiodes outputs with the conditions described on the left figure caption and ellipsoidal fit (orange curve) with the relative fit parameters X_0, X, Y_0, Y and ϕ.

3.3 Spectral Analysis

This section illustrates the steps of the analysis, carried out with a custom Python script, that leads to the calculation of the effective temperature T_{eff} associated with thermal noise, starting from the powers read by the photodiodes ad acquired by the data acquisition system.

3.3.1 Power Spectral Density of the Oscillator Displacement

The minimum displacement δx detectable by the NETN experiment is limited by different noise sources impacting at different frequencies. In order to more easily separate the displacement caused by the longitudinal oscillator vibrations from that, real or apparent, associated with other noise sources, the analysis is conducted in the frequency domain. Therefore, the power spectral density of the measured δx is computed. This PSD can be seen as the sum of an ideal component $S_{\delta x}^{(ideal)}$, only due to the displacement δx, and a contribution S_N due to other noises affecting the measuring apparatus, mainly photodiodes shot noise, ADC limited resolution and residual mechanical noise. Therefore the computed PSD can be expressed as:

$$S_{\delta x}(\nu) = S_{\delta x}^{(ideal)}(\nu) + S_N(\nu) \tag{3.26}$$

This composition of the PSD measured can be seen graphically in the insert of figure 3.3. To calculate $S_{\delta x}(\nu)$, the PDs signals are acquired at the sampling frequency $f_{fast} = 8kHz$ and stored in 20 minutes long files. The signals are corrected based on the calibration parameters acquired at the beginning of the data acquisition according to the procedure described in 3.2.1. The result of the procedure is a calibrated optical phase which is then converted in a displacement δx using equation 3.21. At this point, the whole time-series is divided into segments of duration $T = 20$ seconds, and for each of them the PSD is estimated based on the Fast Fourier Transform of the signal, with a resulting frequency resolution of $\delta f = 1/T = 0.05\,Hz$.

3.3.2 White Noise Selection

Due to the high sensitivity of the experiment, to reject unreliable data due to excessive environmental or acquisition noise, or to bad fit, the spectra are selected based on a series of criteria.

A first selection of the spectra is performed based on the value of the background noise in the kHz region. Here, except for a number of peaks, the noise is almost white and is expected to be associated to the readout chain rather than to actual motion of the system.

A test PSD is produced by averaging the first ~ 6 minutes of the acquired data (see figure 3.3). From this PSD it is possible to identify a frequency region with no resonances or anomalies and before the resonant frequency of the oscillator. In this region, the average white noise level for each of the spectra calculated in 3.3.1 is computed, and the results are displayed on a histogram (fig 3.4).

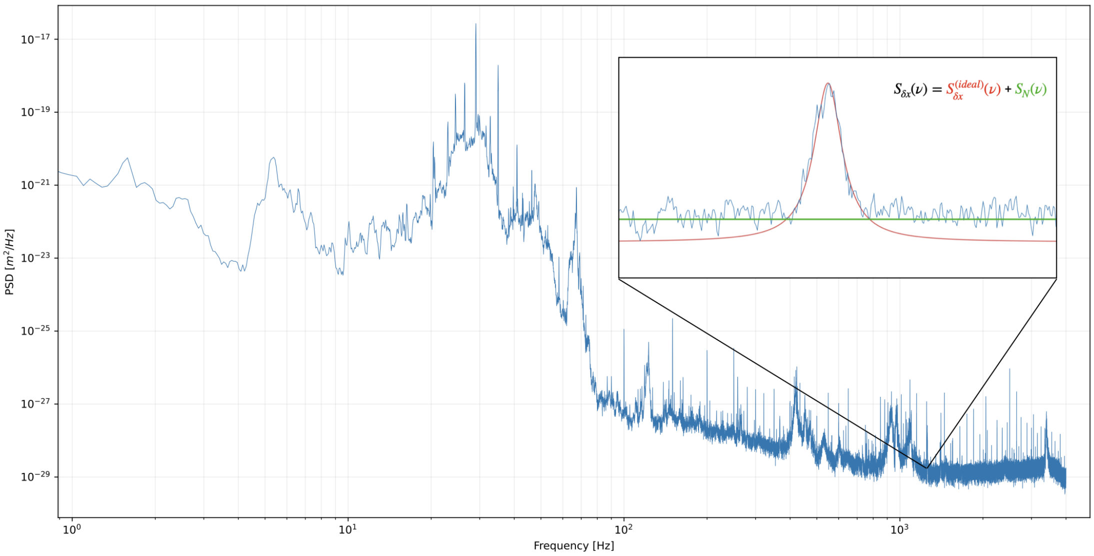

Figure 3.3: Example of a PSD resulting from the average of 20 consecutive PSDs of 20 seconds intervals which have been previously selected (~6 minutes). The structure of the PSD shows higher values at low frequencies, with several peaks between 30Hz and 70Hz, while it decreases toward higher frequencies; this shape is related to the cascade of three mechanical filters that sustain the oscillator (2.2.3). At higher frequencies the PSD is nearly flat and the noise floor is mainly due to photodiodes shot noise and resolution of the acquisition system. The resonance peak at ~1400 Hz is shown in the insert, where the composition of the PSD described in equation 3.26 is illustrated.

By looking at the histogram, a threshold level is chosen in order to cut the noise distribution tail, and spectra with a white noise above the threshold are discarded.

3.3.3 Lorentzian Fit and Effective Temperature Calculation

The estimation of the PSD of a time series carries a large uncertainty (in fact, the variance of every single point in the PSD is equal to the point's value), and this can make it difficult for the non-linear fit routine to converge properly. To reduce this uncertainty, N spectra can be averaged (under the assumption that they are all realization of the same stationary process), reducing the uncertainty on each point by a factor $\sqrt{N}$. To this purpose we average the spectra that passed the previous selection in groups of 20, reducing the statistical fluctuation by a factor ~4.

Each averaged spectrum is then fit in the region corresponding to the longitudinal vibration mode of the oscillator (around 1400 Hz). The extremes of the fit are defined by looking at the same test PSD used to define the interval where to estimate the white noise and change according to

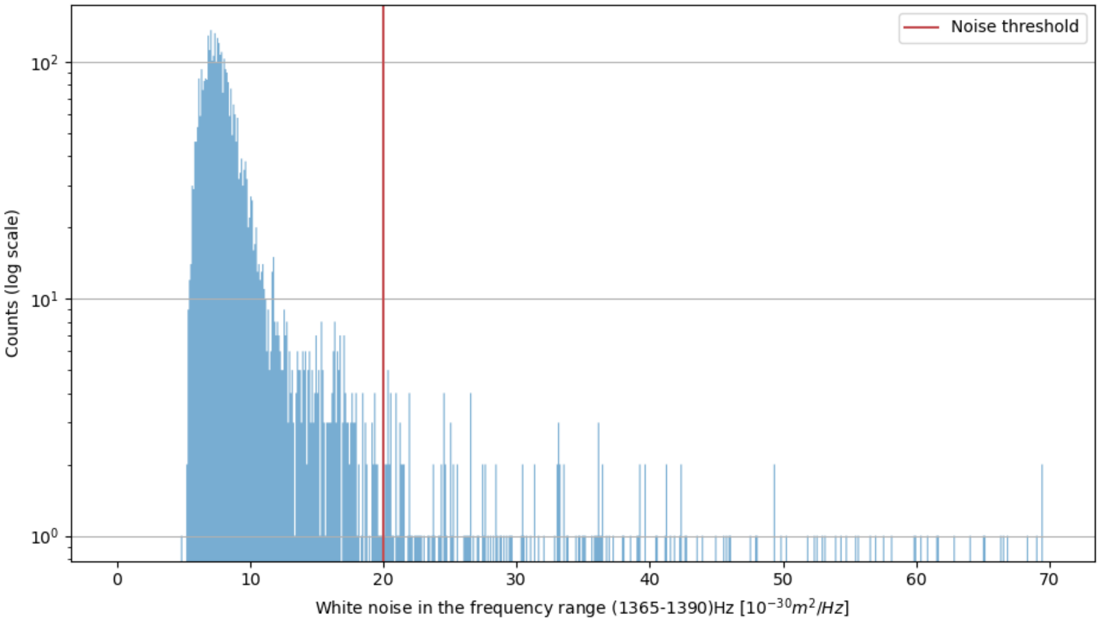

Figure 3.4: Example of histogram of the white noise values calculated in the frequency range (1365-1390)Hz for each 20 seconds PSD of each file considered for the analysis. The red vertical line defines the noise threshold chosen, in this case equal to $20 \times 10^{-30} m^2/Hz$. All the 20 seconds PSDs characterized by a white noise value higher than the threshold (corresponding to the tail of the noise distribution) are discarded by the analysis.

the resonance frequency (in chapter 4 it will be shown that the latter changes over time). These extremes are set to be an interval of ±3 Hz around the value of the resonance frequency. The resonance peak is fitted with the combination of a Lorentzian curve and a constant, which is a good approximation, near the resonance frequency, of the formula 1.22 describing the PSD of the motion of a solid due to thermal noise:

$$y(\nu) = y_0 + \frac{2}{\pi} A \frac{\Delta\nu}{4(\nu - \nu_0)^2 + \Delta\nu^2} \tag{3.27}$$

where the constant y_0 represents the noise level out of resonance, ν_0 the resonance frequency, A the peak area and $\Delta\nu$ the full width at half maximum. Therefore, for each averaged spectrum, A, ν_0, $\Delta\nu$ and an estimation of the white noise are calculated, along with the reduced χ^2 associated to the fit.

At this point another selection is performed by discarding all the fit that are characterized by reduced χ^2 higher than a defined threshold: a fit is rejected if its reduced χ^2_R is higher than a threshold $\chi_R^{2theshold}$, defined such that $P(\chi^2_R > \chi_R^{2theshold}) = 5\%$. An example of the parameters resulting from the fits and of the χ^2_R selection is shown in figure 3.5 (left), where the data passing the selection is indicated in red.

The area A of the Lorentzian curve and the resonance frequency ν_0 of the longitudinal mode, resulting from each fit, are used to calculate an effective temperature with the same formula obtained and used by the RareNoise experiment to infer the thermodynamic temperature from the energy stored in the mode (see section 1.4.2):

$$T_{eff} = \frac{m \cdot (2\pi\nu_0)^2 \langle x^2(t) \rangle}{k_B} \tag{3.28}$$

where $m \sim 0.234kg$ is the mass of the oscillator and $\langle x^2(t) \rangle = A$ is the mean square longitudinal vibration caused by thermal noise. For any given time interval in which the conditions can be considered stationary (and this depends on the type of measurement that is being performed), the distribution of all the calculated effective temperatures is fitted with a Gaussian curve (figure 3.5 (b)), whose mean value $\mu = T_{avg}$ represents the estimation of effective temperature T_{eff} for that particular measurement.

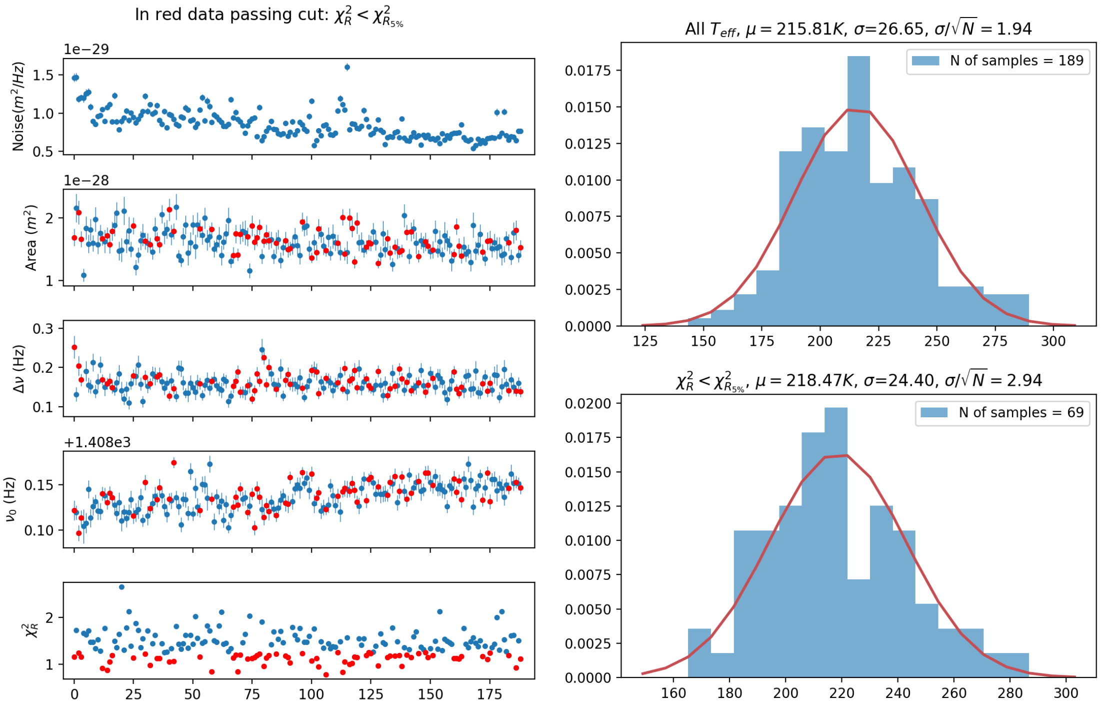

(a) *Parameters of the Lorentzian fits* (b) *Effective temperatures histogram*

Figure 3.5: (a) Parameters of the Lorentzian fits of the longitudinal mode of the oscillator for each selected and averaged spectrum. The x-axis represents the sample count. The data in red represents those that have passed the selection on the reduced χ^2. The plot of the calculated temperature as a function of the fit number is not shown, as it is simply proportional to that of A, given that ν_0 is $\sim$constant. (b) Histogram of the calculated effective temperatures before (up) and after (down) the reduced χ^2 selection. For each histogram the mean value $\mu = T_{avg}$ as well as the standard deviation σ and the reduced standard deviation $\sigma/\sqrt{N}$ are calculated.

Chapter 4

Results and Discussion

This chapter presents the results obtained by the NETN experiment during this thesis work at the Laboratori Nazionali di Legnaro (Padua).

The aim of this experiment coincides with that of the previous RareNoise experiment, i.e. to precisely measure the vibrations of a macroscopic oscillator caused by thermal noise in thermodynamic equilibrium, and subsequently compare them with those measured in a non equilibrium steady state (NESS). The scientific goal is to study the behavior of the thermal noise outside thermodynamic equilibrium and its implications on the energy equipartition principle, both in the prediction of the average energy and in the energy equipartition itself.

What differentiates the NETN experiment from the previous RareNoise is the substitution of the capacitive readout with an interferometric one. The use of an interferometric readout allows to perform an absolute calibration in terms of the oscillator displacements, thus reducing significantly the presence of systematic errors.

In both experiments, the study of thermal noise in and out the thermodynamic equilibrium is carried out through the estimate of the effective temperature $T_{eff} = m\omega^2\langle x(t)^2\rangle/k_B$, where the experimentally obtained quantities are the area $A = \langle x(t)^2\rangle$ of the resonance peak of the vibration mode of interest, and the resonance frequency ω. In fact, in thermodynamic equilibrium and in the absence of external noise sources, according to the equipartition principle, it is possible to estimate the thermodynamic temperature from the energy stored in the mode, i.e. from A. However, this may not be verified in the presence of a NESS. For this reason it is necessary to compare the T_{eff} calculated in and out the equilibrium state.

Experimentally, the comparison between T_{eff} in a NESS and at equilibrium can be done in two ways: relative, simply comparing the uncalibrated signal measured at equilibrium with that measured in a NESS; or absolute, providing first an absolute calibration of the system, and then measuring the level of noise in the two cases. In this last approach, one can check that the T_{eff} is in fact consistent with ambient temperature.

Unfortunately, to date the measurement of T_{eff} in equilibrium showed several problems, despite the improvement of the calibration procedures, characterizations of the optical readout and the mechanical interventions (the latter of which are reported in the section 4.1). The main problems affecting the equilibrium measurements of T_{eff} are a fluctuation of the measured values, with a magnitude that cannot be explained by corresponding fluctuations in the thermodynamic temperature, and the fact that these were always lower than the thermodynamic temperature, which indicates the presence of a systematic error. For these reasons, during this work, no measurements were performed in a NESS.

The focus of the work here presented was instead to identify the cause of the T_{eff} behavior in thermodynamic equilibrium described above. Measurements were first carried out with the acquisition and analysis methods described in section 3.3, to monitor the effect of the mechanical interventions on the T_{eff} measurements. These interventions, as explained in detail in the next section, involve the screws that fix the flange containing the oscillator to the third stage of the mechanical filters. Section 4.1 reports the results of this first study. On the basis of the results obtained, it was decided to start a more systematic and continuous measurement of T_{eff}, in order to investigate the origin of the unexpected behavior of the equilibrium T_{eff}. The results of these latter measurements are reported in section 4.2.

4.1 System Rigidity Test

As anticipated, in the first part of this work mechanical interventions were carried out on the system. This section reports a series of measurements that monitor the system's response to these interventions. These interventions concern the flange that supports the oscillator, together with the reference mirror and the PBS necessary to monitor its vibrations (this system can be seen in figure 2.1 (b)). It has been discovered in the past, by removing the flange, that the eight steel screws holding the flange to the filters (which have been tightened with a torque of 15 Nm) were loose. The original configuration of the flange can be seen in figure 4.1 (a), were the screws aforementioned are circled in red.

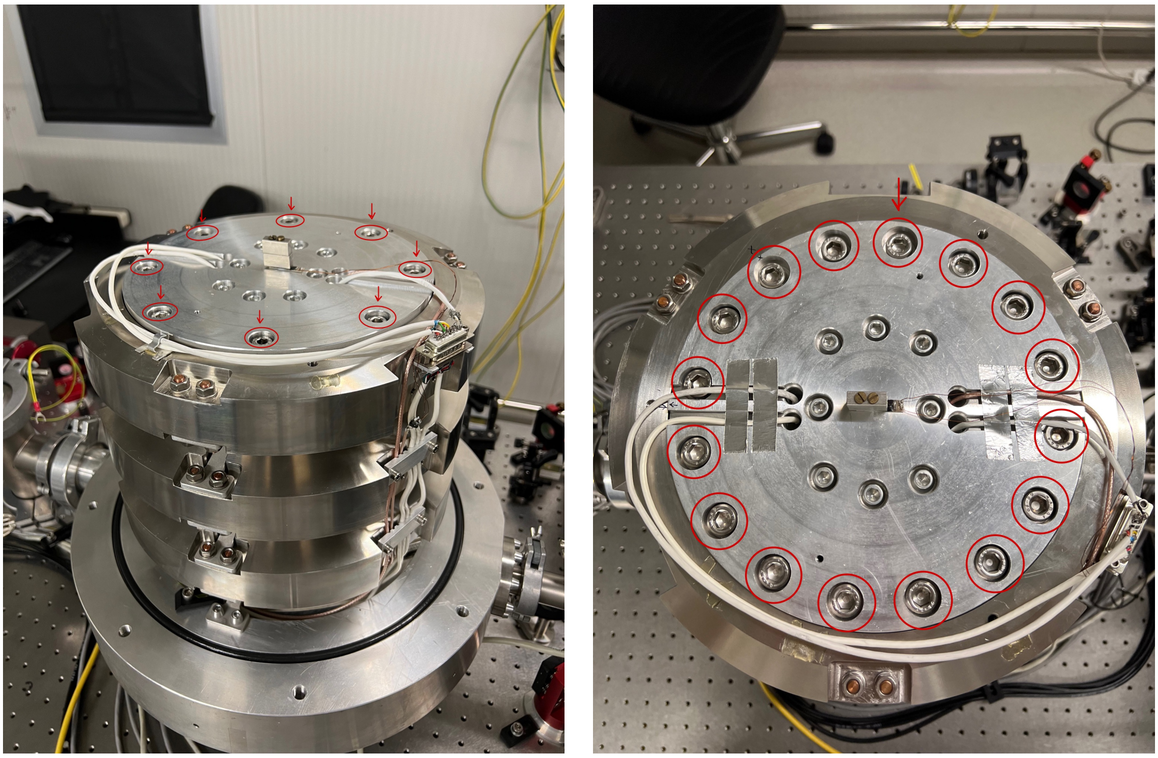

(a) *Original flange*

(b) *Modified flange*

Figure 4.1: (a) Picture of the three mechanical stages usually enclosed in the vacuum chamber. The upper stage contains the flange, to which the oscillator-PBS-reference mirror system is attached. Originally the flange was fixed to the third mechanical filter, as visible here, by eight M8 steel screws, tightened with a torque of 15 Nm. (b) Picture of the flange, fixed to the third mechanical filter, after eight more screw were added and the pre-existing ones were enlarged, for a total of sixteen M10 steel screws, tightened at 20 Nm.

It was not clear whether the screws had loosened over time, after being tightened at 15 Nm, or whether they had been tightened with a lower torque from the beginning. The screws were subsequently repositioned and tightened at 15 Nm. After the system was brought back into operation, a change in the behavior of the measured T_{eff} was observed, which appeared to be more stable over time and closer to the thermodynamic temperature (see initial data in figure 4.2, with white background). This change, however, faded away over time. This behavior motivated a study of the response of T_{eff} at the variation of the state of the screws holding the flange.

For this purpose, measurements have been performed acquiring data overnight (from ∼6 pm to ∼9 am), or over an entire weekend, covering overall a time span of about three months. These moments were chosen for data acquisition as they are favored by the reduced presence of people in the laboratory and in the surrounding areas, which could cause an increase in environmental noise.

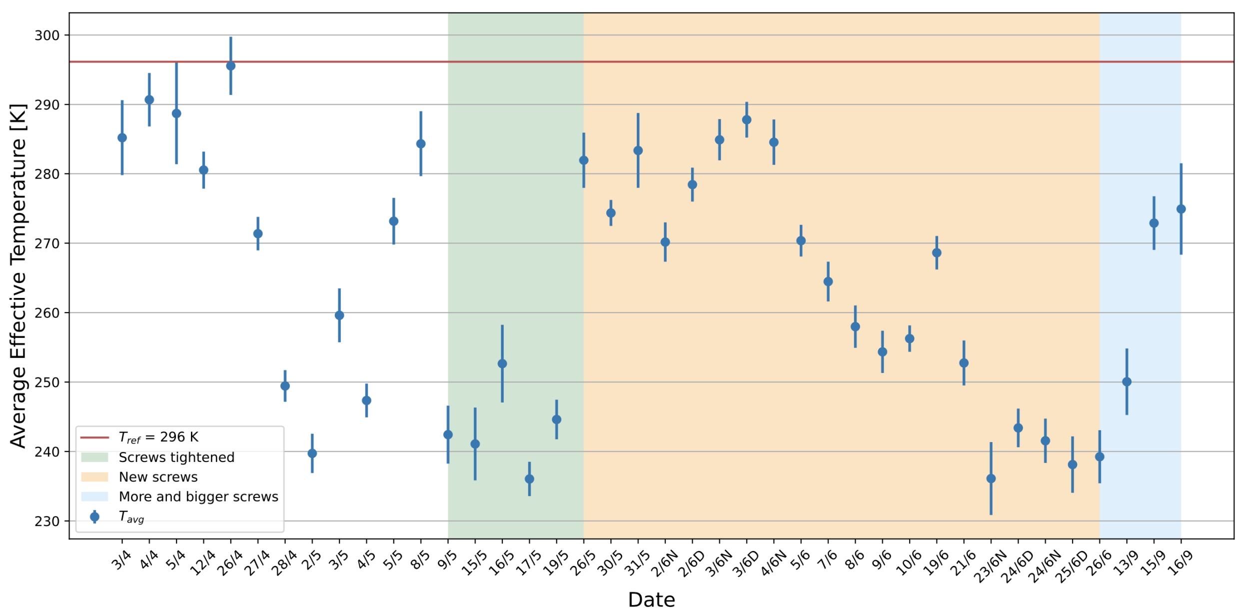

Figure 4.2: Plot displaying the values of T_{avg} calculated by analyzing overnight and weekend acquisitions as described in section 3.3. These measurements cover a period of about three months, as can be seen on the x axis, were the date represents the day when the acquisition started, and full weekend acquisitions have been divided in days and nights (indicated as D and N respectively). The error bar on each value represents the standard deviation of the mean $\sigma/\sqrt{N}$, were N is the number of averaged T_{eff}. The red line on the plot represents a reference of the average ambient temperature $T_{ref} \sim 296$ K (and not a real time measure of the ambient temperature). The different colors indicate a change in the tightening torque of the screws that fix the flange to the third stage of the mechanical filters, or a substitution of them, as explained in the text.

The effective temperatures resulting from performing the data analysis described in section 3.3 on these measurements are displayed in figure 4.2. The plot shows the various T_{avg}, obtained as the average value of the T_{eff} calculated for each spectrum produced in the data analysis for that particular measurement (as seen in figure 3.5) and indicates the date on which the overnight acquisition of the relative measurements started. In the case of a full weekend acquisition, this has been divided in days and nights (indicated as D and N respectively on the plot), due to the limited amount of data that can be analyzed by the computer at one time. The error bar on each value represents the standard deviation of the mean $\sigma/\sqrt{N}$, with N being the number of T_{eff} averaged. The red line on the plot represents a reference of the average ambient temperature $T_{ref} \sim 296$ K. A real time value of the ambient temperature of the laboratory is not present due to a problem in the collection of the slow channel data, but giving that the laboratory is thermally stabilized, it is not expected to vary from the average value by more that a couples of degrees kelvin.

In figure 4.2 different colors denote a change in the the tightening torque of the eight M8 steel screws that fix the flange to the mechanical filters, or a substitution of them.

Until May 8^{th}, the measured T_{avg} showed a significant fluctuation over time, indicating that the effect of tightening the screws described above had already faded. On May 9^{th} the vacuum chamber was opened and the tightening torque verified to be lower than 15 Nm (between 11 and 13 Nm). The screws were tightened again at 15 Nm and the system was brought back into operation. The green section of plot 4.2 reports the measurements performed after this intervention, which do not show the expected improvement. On May 19^{th} the chamber was opened again to verify the tightening of the screws, which were found to be loose again. This time it was also noticed that the screw threads had worn-out, thus all eight screws were substituted with new ones of the same type. The orange section of plot 4.2 reports measurements performed after this substitution.

The measured values of T_{avg} in the orange section not only did not stabilize, but seemed to show a decreasing trend, possibly associated with the loosening over time of the screws even though these were new. This can be attributed to the fact that, although the screws were new, the screw holes were not, and they could have been damaged as well. Furthermore, the screws were tightened to the limit of the torque allowed for their type.

This led to the decision of modifying the experimental apparatus, increasing the number of screw holes on the flange and widening the pre-existing ones, such that the flange and the third stage mechanical filter could be kept together by a total of sixteen M10 steel screws, screwed with a torque of 20 Nm. The flange after this modification can be seen in figure 4.1 (b). The blue section of plot 4.2 reports the measurements performed in this new configuration. These T_{avg} measurements continued to be sub-thermal and to show fluctuations (as confirmed by further measurements reported in section 4.2).

The variation of the resonance frequency ν_0 and of the FWHM of the resonance peak ($\Delta\nu$) over the whole period are reported in figure 4.3. This plot reports an average value of the two quantities for each measurement, distinguishing with the same colors of figure 4.2 the different configurations of the flange. What can be seen from the plot is that the resonance frequency changes at each change of the configuration. The first time the screws are tightened (green) ν_0 slightly decrease: this is somewhat surprising, since one would expect the resonance frequency to increase with increase rigidity of the system, which is confirmed by the subsequent measurements. In this case, it could be that the already worn-out threads were actually further degrading and loosing grip as the screws where tightened.

When the screws are replaced with new ones instead (orange section) an increase is visible, from ~ 1399 to ~ 1402 Hz. This is a sign that by replacing the screws with new ones the rigidity of the structure increased. As expected, when more and bigger screws substitute the eight original ones the rigidity of the structure increases significantly, given a resonance frequency increase of ν_0 of ~ 6 Hz. The FWHM instead remained almost constant around ~ 0.45 Hz, until the replacement of the eight M8 screws with the sixteen M10 screws, were it reached the value of ~ 0.2 Hz. This indicates overall an increase in the quality factor $Q = \nu_0/\Delta\nu$ by almost a factor 2 by modifying the flange.

The persistence of fluctuations in the trend of the measured T_{avg}, despite improving the flange configuration (as confirmed by the increased resonance frequency of the oscillator longitudinal mode), led to the conclusion that the non-rigidity of the system was not the only factor influencing the unexpected behavior of T_{avg}.

4.2 Continuous Measurements

From the study reported in the previous section it was concluded that the problem of fluctuations in the T_{eff} measurement was not due to the insufficient rigidity of the system, or not only to that.

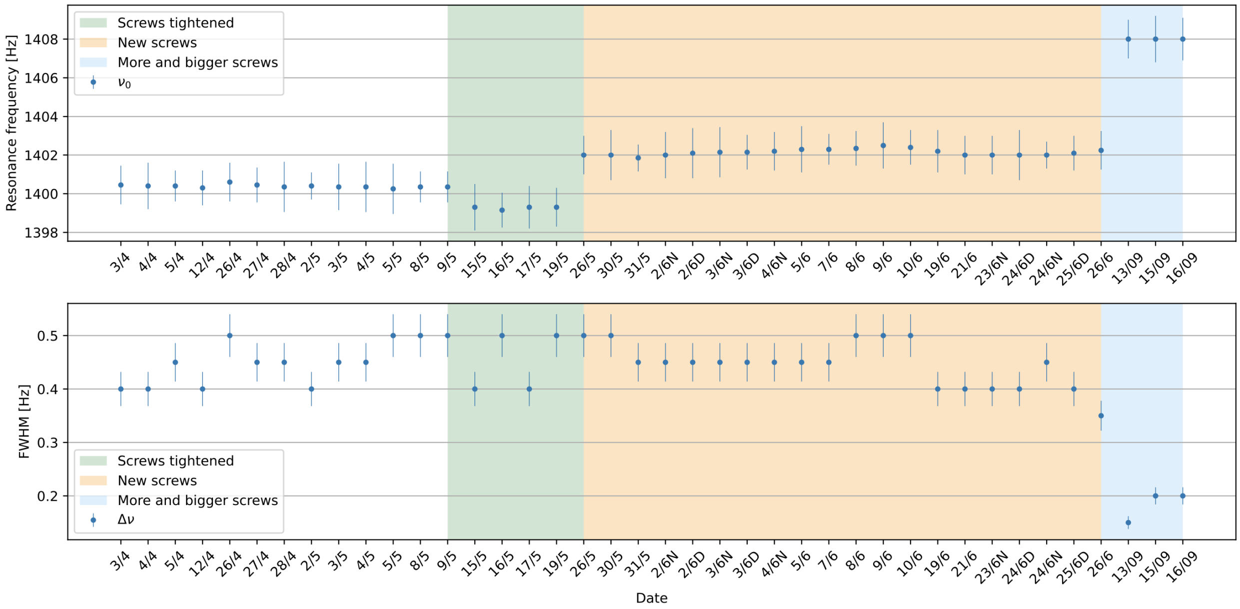

Figure 4.3: Plot of the average resonance frequency and FWHM of the resonance peak associated to each overnight measurement. Different colors distinguish the different configurations of the flange, as explained in the text.

In order to investigate the origin of the unexpected behavior of the equilibrium T_{eff}, it was decided to start a different data acquisition campaign, in order to continuously monitor the system and to allow a statistical analysis of the results. For this purpose, the Lab View acquisition program was modified so that it could continuously acquire one hour of data followed by a three-hour break. It was necessary to modify the acquisition program due to the limited memory of the computer linked to the acquisition system. During the acquisitions the condition of the setup remained unchanged. It was possible in this way to acquire measurements continuously and analyze the trend of the resulting T_{avg} week by week. A calibration was acquired every week to verify that the system remained aligned over time. If slight misalignments were present, a calibration was collected both before and after the realignment procedures. The values of T_{avg} measured during this continuous acquisition are reported in the bottom plot of figure 4.4.

Furthermore, for a more detailed study of the temperature trend, it was decided to plot not only T_{avg}, but also the value of T_{eff}, calculated as in equation 3.28, associated to each spectrum selected and averaged as described in section 3.3. The measured values of T_{eff} are reported in the middle plot of figure 4.4. From both the plot of T_{avg} and T_{eff} it is visible a high variability, not justifiable with the sole variation of thermodynamic temperature. The effective temperature fluctuates around 270 K between September 18^{th} and 22^{th}, then a rapid drift brings it around 200 K until September 30^{th}, when it moves again rapidly towards 250 K, where it remains almost stable until the end of the acquisition. Then not only the measured T_{eff} continued to result sub-thermal, but it kept also showing relatively big oscillations, due to phenomena that are currently unknown.

Along with T_{eff}, other quantities usually derived by the analysis have been displayed and studied. This allowed to study the correlations between all the variables used in the data analysis to estimate T_{avg}: the resonance frequency ν_0, the FWHM of the resonance peak ($\Delta\nu$), the white noise value (N_{fit}) estimated by fitting the resonance peak of each produced spectrum, the white noise value (N_{avg}) estimated averaging the displacement PSD in a range of frequencies before the resonance (as seen in 3.3.2) and the average phase ϕ indicative of the working point. This continuous monitoring lasted about one month.

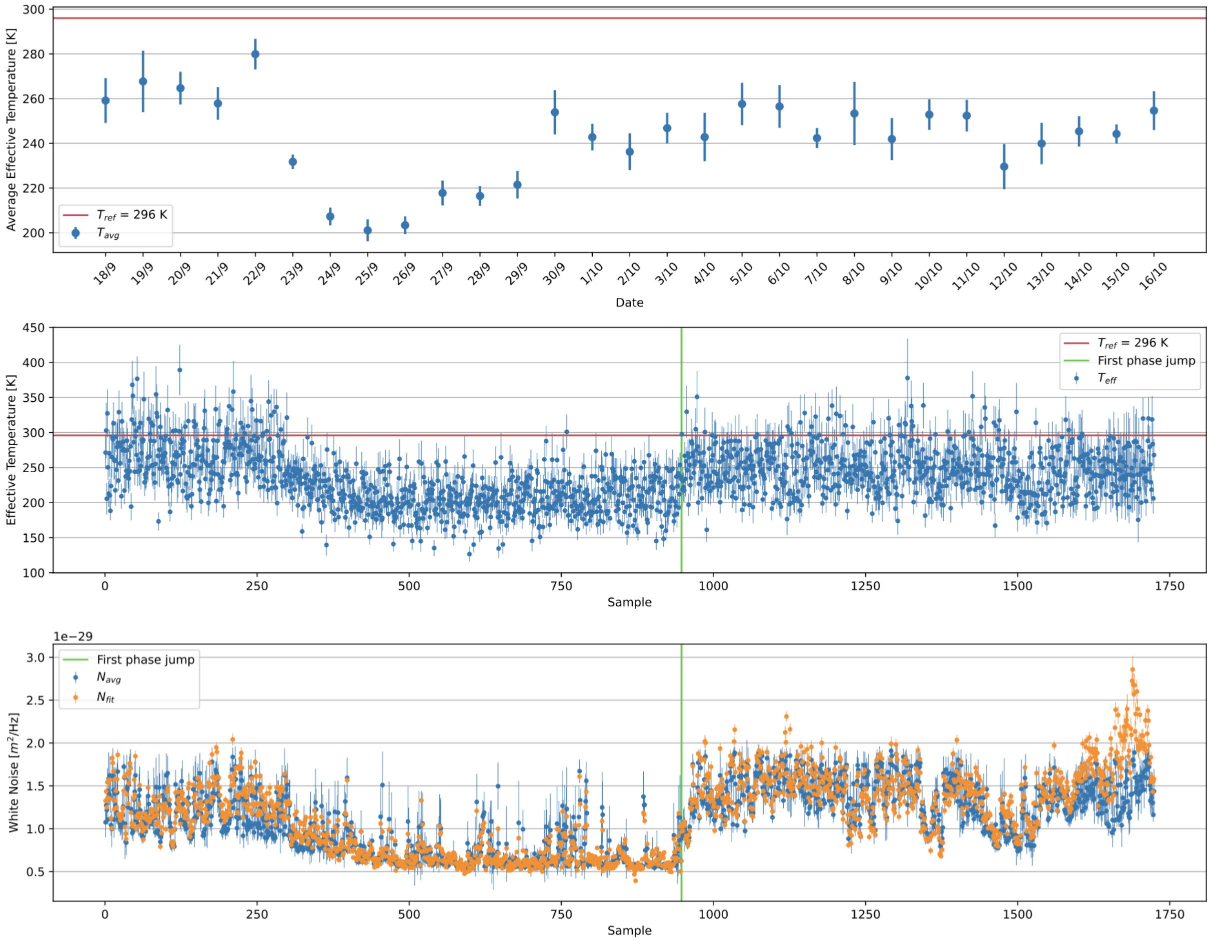

Figure 4.4: TOP: plot of the T_{avg} obtained by averaging the effective temperatures measured each day. The error bar is derived as the standard deviation of the mean $\sigma/\sqrt{N}$. MIDDLE: plot of the T_{eff} calculated with 3.28 for each spectra produced, selected and averaged by the analysis (as seen in section 3.3). The x axis represents a sample count and not a time unit. For a rough time reference see the upper plot. The error bar associated to each value is derived by propagation of the errors associated to A and ν_0. In both plots an average ambient temperature T_{ref} is indicated as a reference with a red horizontal line. It does not provide a real time measure of the ambient temperature. BOTTOM: plot of the two white noise estimates: N_{avg} (blue) and N_{fit} (orange). The errors associated to N_{avg} and N_{fit} are respectively the standard deviation of the mean (relative to the averaged spectra) and the standard deviation calculated by the fit. The x axis represents the sample count.

All these quantities were collected in order to identify possible correlations between them, which could provide useful information to explain the trend of T_{eff} shown in figure 4.4. To do so, each quantity had to be sampled or averaged with the same frequency, so that one could be plotted against the other. For this purpose, N_{avg} and ϕ were reprocessed to match the sampling of the quantities resulting from the Lorentzian fits, i.e. in such a way that to each selected and averaged spectrum corresponded a single N_{avg} and ϕ value. For N_{avg}, which was originally calculated for each 20 seconds spectra (see section 3.3.2), it was sufficient to apply the same operations of selection and averaging that had been performed to obtain the spectra to be eventually fitted.

The values of the interferometer phase ϕ are computed from the output of the four photodiodes with a sampling rate of 8 kHz. A single value of ϕ for each 20 seconds spectrum was obtained by averaging the values measured in those 20 seconds, only to be then processed in the same way as N_{avg}.

For each couple of variables the Spearman's correlation coefficient was calculated [28], which assesses how well the relationship between two variables can be described using a monotonic function. This type of correlation was chosen so as not to limit the research to linear correlations, such as the ones quantified by the Pearson's correlation coefficient. By building a matrix with these calculated coefficients, visible in figure 4.5, it is possible to identify correlations between several quantities: some can be explained easily while others came out as unexpected.

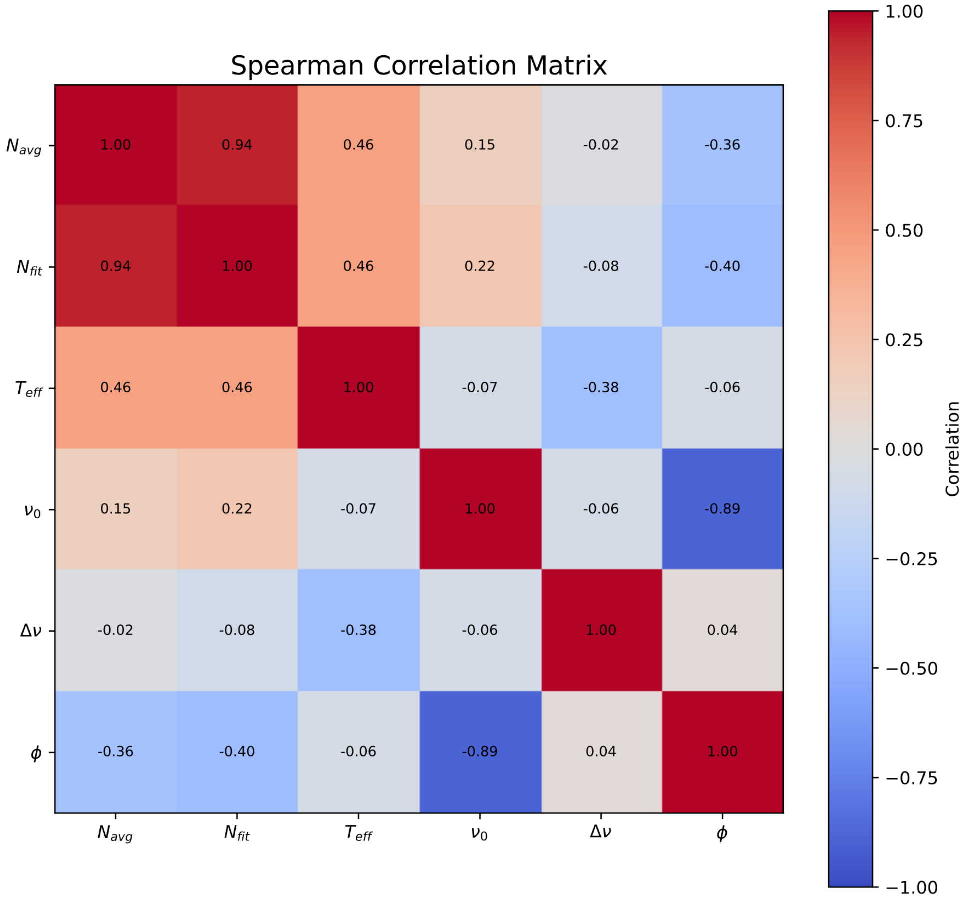

Figure 4.5: Spearman correlation matrix of the six quantities considered in this analysis: N_{avg}, N_{fit}, T_{eff}, ν_0, $\Delta\nu$ and ϕ. For each couple of quantities the Spearman's rank correlation coefficient is indicated inside the relative square. This coefficient assesses how well the relationship between two variables can be described using a monotonic function. In the estimation of the correlation of other variables with ϕ, the latter was unwrapped.

Among the expected correlations is the one between the two different white noise estimates considered in the analysis: N_{avg} and N_{fit}. As can be seen from the matrix in 4.5, the Spearman's correlation coefficient between N_{avg} and N_{fit} is equal to 0.94, indicating that the estimation procedures are consistent, and suggesting therefore their goodness. A plot of the two noise estimates during the monitoring is reported in the bottom plot of figure 4.4, from which the correlation between the two parameters is clear, but it is also visible a high variability in their trend.

Another expected (anti)correlation is the one of the resonance frequency ν_0 with the phase ϕ, indicative of the working point. The Spearman's correlation coefficient between these two quantities is equal to -0.89. In the calculation of this correlation coefficient ϕ has been unwrapped. This correlation is also shown in figure 4.7, where ν_0 is plotted against the unwrapped ϕ, and in figure 4.6, were the trend of both quantities during the period in analysis is visible. The correlation between these two quantities is physically correct and expected, since both are linked to the thermodynamic temperature (ambient temperature inside the laboratory): if the thermodynamic temperature changes, the two arms of the interferometer, defined by different material and geometries, will undergo a different thermal expansion and cause a change in the working point ϕ. At the same time a temperature change affects also ν_0, as an increase in the temperature softens the oscillator's material, decreasing ν_0, and vice versa.

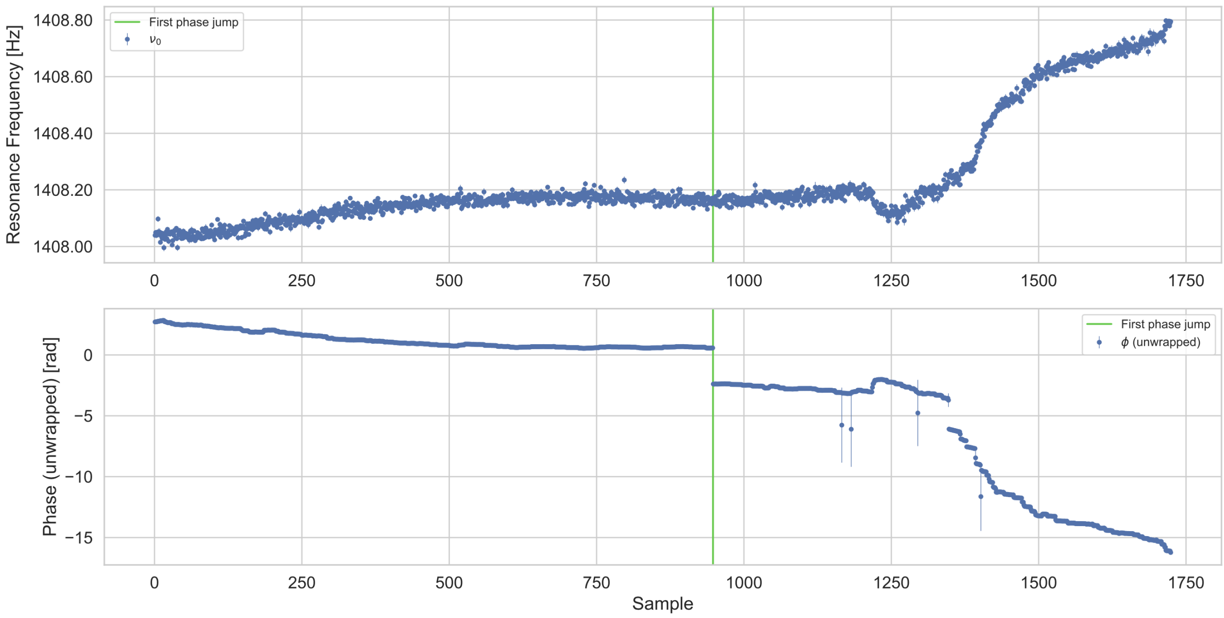

Figure 4.6: TOP: plot of the resonance frequency ν_0 over sample number. The error associated to each value is the standard deviation calculated by the fit. BOTTOM: plot of the unwrapped phase ϕ over the sample number. The error associated to each value is the standard deviation of the mean (relative to the averaged spectra). The vertical green line indicates one of the two phase jumps visible on the plot. This first jump is highlighted as it seems to be correlated to a jump also in the T_{eff} plot and in the noise plot (figure 4.4).

From figure 4.5 it can also be seen that T_{eff} and ϕ are not correlated (with a Spearman's correlation coefficient of -0.06). This demonstrates that the measured temperature is independent of the working point, as one would want it to be.

At the same time, N_{avg} and N_{fit} results to be correlated with the working point ϕ, with a Spearman's correlation coefficient of -0.36 and -0.40 respectively. This is visible also in the plot in figure 4.8, where the two noise estimate are plotted against the unwrapped ϕ. This correlation represents something unexpected and unwanted in the experiment. However, it can be explained in many ways, all equally plausible, such as one of the photodiodes being more affected by optical-electronic noise than the other three. In this way, the total noise on the recorded signal would indeed depend on the working point. Further tests are needed to verify whether this or other similar hypotheses are the cause of this correlation.

Another unexpected correlation is the one of T_{eff} with the two noise estimates N_{avg} and N_{fit}, with a Spearman's correlation coefficient of 0.46 in both cases. This is visible also in figure 4.4, where the plot of the two quantities seems to follow the same trend. Considering that this correlation cannot be due to the working point, that has been shown to affect the noise but not T_{eff}, this

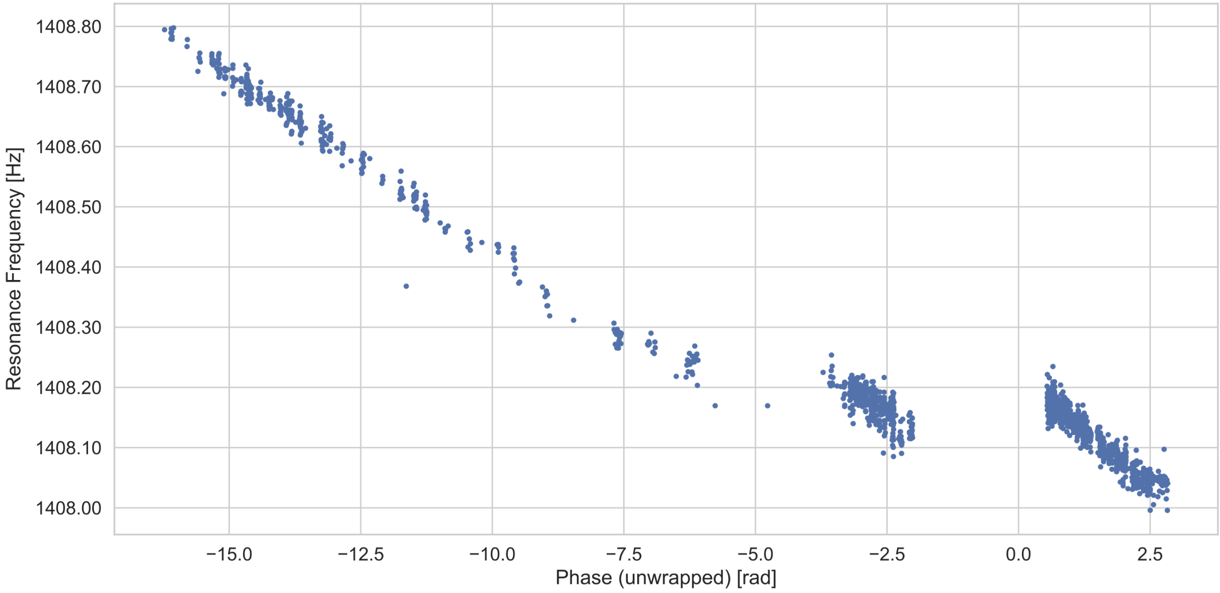

Figure 4.7: Plot of the resonance frequency ν_0 in function of the unwrapped phase ϕ. The jump between values ∼-2.5 rad and ∼0 rad is the one indicated in the other diagrams with a green vertical line.

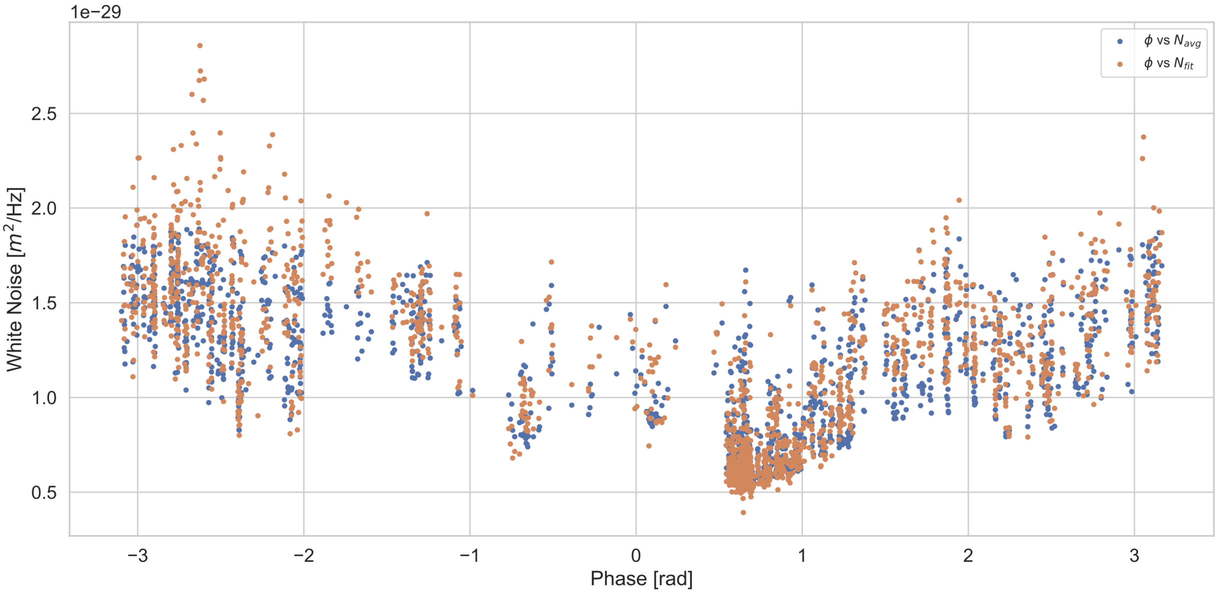

Figure 4.8: Plot of the white noise estimations N_{avg} (blue) and N_{fit} (orange), as a function of ϕ, i.e. of the working point. It this plot ϕ is not unwrapped to make the correlation is more evident.

suggests that there must be some other parameter that affects both T_{eff} and the noise. This cannot have a physical origin, as the white noise is related to the readout system and not to real motion of the oscillator, and it is unlikely to be a consequence of the fitting procedure giving that N_{avg} is not obtained from the fit. However this hypothesis cannot be excluded yet. Further studies are necessary to understand whether the cause of this unwanted correlation is to be found in the interferometric readout, in a problem with the data acquisition system, in the fitting procedure or in other hypotheses not been taken into consideration yet.

Another issue arises by noticing two jumps in the trend of the working point ϕ. The first of these jumps is highlighted with a green vertical line in figure 4.6. This event is not in itself noteworthy; however it seems to coincide with a quick drift in the T_{eff} and white noise trends as well, indicated in figure 4.4 with the same green vertical line to highlight the correlation. It is important to notice that this event does not induce instead a jump in the ν_0 trend (as can be seen in 4.6), indicating that it is not caused by a change in the oscillator characteristics. Further tests are needed to understand the origin of this event and how could it induce a common change in quantities, such T_{eff} and ϕ, that otherwise not correlated, as shown in figure 4.5.

This analysis was useful to verify some aspects such as the validity of the two white noise estimates, or the expected correlation between ν_0 and ϕ, but also for bringing to light unexpected relationships between some parameters of the experiment. Through further tests and studies, these correlations could lead to understanding what influences the trend of T_{eff}, apart from the thermodynamic temperature, and causes the observed fluctuations.

Conclusions

The scientific motivation of the work reported in this thesis is the study of the thermal noise effects in a macroscopic oscillator, both in and out thermodynamic equilibrium. The high precision measurements of the thermal noise-induced vibrations have been carried out with a quadrature phase differential interferometer, in which the macroscopic oscillator represented one of the interferometer's mirrors. However, in thermodynamic equilibrium, in which thermal noise can be predicted by theory, the estimated amplitude of thermal noise induced oscillations resulted to be lower than the one expected from theory, and was characterized by relatively high fluctuations, not explainable by the sole variation of thermodynamic temperature. This behavior prevented from carrying out measurements outside the thermodynamic equilibrium (by imposing a NESS), due to the lack of a stable reference in the equilibrium measurements.

Therefore this work focused on the measurement of thermal noise in equilibrium, and in particular on investigating the reasons for the mentioned behavior, with the aim of obtaining measurements in equilibrium in agreement with the theory and without any free parameters, and then being able to compare them with a non-equilibrium ones.

The amplitude of the thermal noise induced vibrations was associated with an estimated effective temperature T_{eff}. The measurements of T_{eff} were first studied in different mechanical conditions of the system; in particular, the initial hypothesis was that the variation of its overall rigidity due to the loosening of some screws could cause the observed unexpected behavior. After some modifications of the apparatus to ensure that it maintained rigidity over time, these fluctuations did not disappear, indicating that this was not the cause of this behavior, or at least not the only one.

It was therefore decided to monitor the system almost continuously over time, and to analyze the correlation between various quantities including, in addition to T_{eff}, the white noise affecting the measurements, the working point ϕ and the resonance frequency ν_0 of the vibration mode considered. Among the various correlations found some are justifiable in physical therms while others are not. The most puzzling and maybe critical is the correlation between T_{eff} and white noise, which is not explained by a physical phenomena and therefore was not expected, but that could lead to a common cause of the fluctuations detected in the monitoring of these two quantities.

The next steps of this experiment will be to investigate the origin of this correlation, considering for example the interferometric readout or the data acquisition system, among other hypothesis. Once the problem is identified and fixed, allowing to obtain a measurement of thermal noise in equilibrium in accordance with the fluctuation-dissipation theorem, the experiment will be ready for studying its behavior outside thermodynamic equilibrium.

Bibliography

[1] A. Einstein, *Approximative Integration of the Field Equations of Gravitation*, Sitzungsberichte der Königlich Preussischen Akademie der Wissenschaften, 688-696 (1916)

[2] O. D. Aguiar, *The Past, Present and Future of the Resonant-Mass Gravitational Wave Detectors*, Research in Astronomy and Astrophysics 11, 1–42 (2010) https://doi.org/10.48550/arXiv.1009.1138

[3] R. A. Hulse, J. H. Taylor, *Discovery of a pulsar in a binary system*, Astrophys. J., Lett., v. 195, no. 2, pp. L51-L53 (1975) https://www.osti.gov/biblio/4215694

[4] B. P. Abbott et al., *Observation of Gravitational Waves from a Binary Black Hole Merger*, Phys. Rev. Lett. 116, 6, 061102 (2016) https://link.aps.org/doi/10.1103/PhysRevLett.116.061102

[5] J. Weber, *Detection and Generation of Gravitational Waves*, Phys. Rev., 117, 1, 306-313 (1960) https://link.aps.org/doi/10.1103/PhysRev.117.306

[6] J. Weber, *Evidence for Discovery of Gravitational Radiation*, Phys. Rev. Lett. 22, 24, 1320-1324 (1969) https://link.aps.org/doi/10.1103/PhysRevLett.22.1320

[7] M. Cerdonio, M. Bonaldi, D. Carlesso, E. Cavallini, S. Caruso, A. Colombo, P. Falferi, G. Fontana, P. L. Fortini, R. Mezzena, A. Ortolan, G. A. Prodi, L. Taffarello, G. Vedovato, S. Vitale and J. P. Zendri, *The ultracryogenic gravitational-wave detector AURIGA*, Classical and Quantum Gravity, 14, 6, 1491 (1997) https://dx.doi.org/10.1088/0264-9381/14/6/016

[8] F. Marin, F. Marino, M. Bonaldi, M. Cerdonio, C. Livia, P. Falferi, R Mezzena, A. Ortolan, G. A. Prodi, L. Taffarello, G. Vedovato, A. Vinante, J. P. Zendri, *Investigation on Planck scale physics by the AURIGA gravitational bar detector*, New Journal of Physics, 16, 8, 085012 (2014) https://dx.doi.org/10.1088/1367-2630/16/8/085012

[9] M. Pitkin, S. Reid, S. Rowan, and J. Hough, *Gravitational Wave Detection by Interferometry (Ground and Space)*, Living Reviews in Relativity, 14, 1 (2011) http://dx.doi.org/10.12942/lrr-2011-5

[10] A. Freise, K. Strain, *Interferometer Techniques for Gravitational-Wave Detection*, Springer Science and Business Media LLC, 13, 1 (2010) http://dx.doi.org/10.12942/lrr-2010-1

[11] M. Maggiore, *Gravitational Waves - Volume 1 - Theory and Experiments*, Oxford University Press (2008)

[12] N. Yunes, X. Siemens, *Gravitational-Wave Tests of General Relativity with Ground-Based Detectors and Pulsar-Timing Arrays*, Living Reviews in Relativity, 16, 1, (2013) http://dx.doi.org/10.12942/lrr-2013-9

[13] T. Li, F. Anguilar Sandoval et al., *Measurements of mechanical thermal noise and energy dissipation in optical dielectric coatings*, Physical Review D, 89, 9 (2014) http://dx.doi.org/10.1103/PhysRevD.89.092004

[14] D. Lumaca, *Thermal noise reduction for future gravitational wave detectors*, J. Phys. Conf. Ser., 1226, 1, 012023 (2019) 10.1088/1742-6596/1226/1/012023

[15] P. R. Saulson, *Thermal noise in mechanical experiments*, Phys. Rev. D, 42, 8, 2437–2445 (1990) https://link.aps.org/doi/10.1103/PhysRevD.42.2437

[16] Y. Levin, *Internal thermal noise in the LIGO test masses: A direct approach*, Physical Review D, 57, 2, 659–663 (1998) http://dx.doi.org/10.1103/PhysRevD.57.659

[17] B. Ferrero and L. Bellon, *Harmonic calibration of quadrature phase interferometry*, Europhysics Letters 139, 55002 (2022) 10.1209/0295-5075/ac8761

[18] Peter L. M. Heydemann, *Determination and correction of quadrature fringe measurement errors in interferometers*, Appl. Opt. 20, 3382-3384 (1981) https://doi.org/10.1364/AO.20.003382

[19] L. Conti, P. De Gregorio, *Elasticity of mechanical oscillators in nonequilibrium steady states: Experimental, numerical, and theoretical results*, Phys. Rev. E 85, 066605 (2012) 10.1103/PhysRevE.85.066605

[20] L. Conti, M. Bonaldi, L. Rondoni, et al. *RareNoise: non-equilibrium effects in detectors of gravitational waves, Classical and Quantum Gravity* 27, 084032 (2010) 10.1088/0264-9381/27/8/084032

[21] M. Saraceni, M. Bonaldi, L. Castellani, L. Conti, A. B. Gounda, S. Longo, M. Pegoraro, *A compact, passive setup for low vibration noise measurements in the frequency band (300-2000) Hz*, Rev Sci Instrum. 81, 035115 (2010) 10.1063/1.3361040

[22] L. Conti, P. De Gregori, G. Karapetyan, C. Lazzaro, and M. Pegoraro, M. Bonaldi, L. Rondoni, *Effects of breaking vibrational energy equipartition on measurements of temperature in macroscopic oscillators subject to heat flux*, Journal of Statistical Mechanics: Theory and Experiment 12, P12003 (2013) https://doi.org/10.48550/arXiv.1305.5084

[23] M. Geitner, F. Aguilar Sandoval, E. Bertin, L. Bellon, *Low thermal fluctuations in a system heated out of equilibrium*, Phys. Rev. E 95, 032138 (2017), https://doi.org/10.1103/PhysRevE.95.032138

[24] F. Anguilar Sandoval, M. Geitner, E. Bertin, L. Bellon, *Resonance frequency shift of strongly heated micro-cantilevers*, 117, 23 (2015) http://dx.doi.org/10.1063/1.4922785

[25] A. Fontana, *Thermal fluctuations in an out-of equilibrium system*, Doctoral thesis, University of Lyon (2020)

[26] V. Gualani, *Design and Development of a LISA photoreceiver and Optical Ground Support Equipment (OGSE).*, Master Thesis (2020) 10.13140/RG.2.2.18089.62561

[27] L. Conti, P. De Gregorio, M. Bonaldi, A. Borrielli, M. Crivellari, G. Karapetyan, C. Poli, E. Serra, R. K. Thakur, L. Rondoni, *Elasticity of mechanical oscillators in nonequilibrium steady states: Experimental, numerical, and theoretical results*, Phys. Rev. E, 85, 6, 066605 (2012) 10.1103/PhysRevE.85.066605

[28] R. Artusi, P. Verderio, E. Marubini, *Bravais-Pearson and Spearman Correlation Coefficients: Meaning, Test of Hypothesis and Confidence Interval.*, The International Journal of Biological Markers, 17, 2, 148-151 (2002) doi:10.1177/172460080201700213